

DISCLAIMER NOTICE



THIS DOCUMENT IS BEST
QUALITY AVAILABLE. THE COPY
FURNISHED TO DTIC CONTAINED
A SIGNIFICANT NUMBER OF
COLOR PAGES WHICH DO NOT
REPRODUCE LEGIBLY ON BLACK
AND WHITE MICROFICHE.

ON THE ORIGINS OF LOW-LEVEL TORNADIC CIRCULATIONS
WITHIN THE REMNANTS OF HURRICANE ANDREW

A Thesis

Presented in Partial Fulfillment of the Requirements for
the degree Master of Science in the
Graduate School of The Ohio State University

by

Steven Thomas Fiorino, B.S.

The Ohio State University

1993

Master's Examination Committee:

John N. Rayner

Jeffery C. Rogers

Approved by

Jay S. Hobgood
Advisor
Atmospheric Sciences Program

THEESIS ABSTRACT

THE OHIO STATE UNIVERSITY
GRADUATE SCHOOL

NAME: Fiorino, Steven Thomas

QUARTER/YEAR: Au 93

DEPARTMENT: Geography

DEGREE: M.S.

ADVISOR'S NAME: Hobgood, Jay S.

TITLE OF THESIS: On the Origins of Low-level Tornadic Circulations within the Remnants of Hurricane Andrew

A literature review establishes a key characteristic of tornadic hurricane environments to be the highly sheared lowest 1500 m. The thesis proposes that the shear-produced horizontal vorticity is turned vertical mainly via vertical velocities induced by mass convergence in boundary layer windshift zones, rather than by buoyant updrafts. A two-dimensional mass continuity and convective available potential energy analysis is performed on data from a profiler and acoustic sounder exposed to Hurricane Andrew's tornadic remnants. This analysis suggests the presence of a convergence-produced 5 m s^{-1} updraft at a windshift in the thermodynamically stable boundary layer of a tornadic rainband.

Accession For	
NTIS GRA&I	<input checked="" type="checkbox"/>
DTIC TAB	<input type="checkbox"/>
Unannounced	<input type="checkbox"/>
Justification	
By _____	
Distribution _____	
Availability Codes	
Avail and/or	Special
Dist	
A-1	

DTIC QUALITY INSPECTED 5

Jay S. Hobgood
Advisor's Signature

ACKNOWLEDGEMENTS

I wish to thank Dr. Eugene McCaul, Jr. of the University Space Research Association (Huntsville, AL) and Dr. Kevin Knupp of the University of Alabama in Huntsville. Dr. Knupp took time out of his tight schedule to meet with me and provide me the profiler and sounder data that appear in this work. Dr. McCaul also rearranged his time to allow a personal meeting and provided valuable insights into the phenomena of hurricane-spawned tornadoes. I thank Mr. Walter Snell of the Montgomery National Weather Service station for kindly offering me copies of his slides of the Doppler radar. I especially appreciate Capt. Warren Madden of the 645th Weather Squadron, Wright-Patterson AFB, OH for permitting me the use of his low-level skew-T program and for being a quick link to data from the USAF Environmental Technical Applications Center. My advisor, Dr. Jay Hobgood, deserves special note for being the best instructor I have known and a most cooperative and encouraging mentor. I am grateful to the United States Air Force for allowing me this educational opportunity. Finally, I thank my wife, Lisa, whose love, support and completion of her own thesis two months prior to mine created a stable, goal-oriented work environment.

VITA

January 26, 1965 Born - Wright-Patterson AFB,
Dayton, Ohio

1987 B.S. Geography, The Ohio State
University, Columbus, Ohio.
Commissioned 2nd Lieutenant in
U.S. Air Force

1989 B.S. Meteorology, Florida
State University, Tallahassee,
Florida

1989-1992 Wing Weather Officer, 319th
Bomb Wing, Grand Forks AFB,
Grand Forks, North Dakota

1992-Present Air Force Institute of
Technology at The Ohio State
University, Columbus, Ohio

FIELD OF STUDY

Major Field: Atmospheric Sciences
Emphasis on dynamics of atmospheric systems

TABLE OF CONTENTS

ACKNOWLEDGEMENTS	ii
VITA	iii
LIST OF TABLES	vi
LIST OF FIGURES	vii
LIST OF PLATES	x
CHAPTER	PAGE
I. INTRODUCTION	1
II. LITERATURE REVIEW	4
A. Structure and Characteristics of Hurricanes that Spawn Tornadoes	4
B. Structure and Characteristics of Tornadoes Spawned by Hurricanes	8
C. Applicable Great Plains Tornado Research	9
D. Summary and Comments for the Literature Review	12
III. METHODOLOGY	13
A. What Is Needed	13
B. The Sources	14
C. Analysis Methods	16

IV. DATA AND ANALYSIS	17
A. Hurricane Andrew	17
B. Observations of the Data	19
C. Analysis	38
D. Discussion of Results	53
V. SUMMARY AND CONCLUSIONS	61
LIST OF REFERENCES	64

LIST OF TABLES

TABLE	PAGE
1. First rainband height vs. time values of vertical velocity calculated assuming an incompressible atmosphere (top) and calculated allowing RASS-derived density variations (bottom). Speeds are in m/s and positive values indicate upward motions	50
2. Second rainband height vs. time values of vertical velocity calculated assuming an incompressible atmosphere (top) and calculated allowing RASS-derived density variations (bottom). Speeds are in m/s and positive values indicate upward motions	51

LIST OF FIGURES

FIGURE	PAGE
1. Track of Hurricane Andrew and associated tornadoes indicated by Fujita scale. From Ostby and Weiss (1993)	18
2. Time-height cross section of vertical beam signal-to-noise ratio (dB) for the period 1615 UTC 27 Aug to 0015 UTC 28 Aug 92. The boxed-in area indicates the encounter with the most severe section of the second rainband. From McCaul et al. (1993)	24
3. Time-height cross section of first rainband winds. Full barb indicates speeds of 5 m/s and half barb 2.5 m/s	26
4. Time-height cross section of second rainband winds. Full barb indicates speeds of 5 m/s, half barb 2.5 m/s, and a pennant 25 m/s	27
5. East-west cross section (looking north) of first rainband hydrometeor fall speeds. Speeds in m/s and negative values indicate downward motions ...	29
6. East-west cross section (looking north) of second rainband hydrometeor fall speeds. Speeds in m/s and negative values indicate downward motions ...	30
7. RASS-derived virtual temperature profile (solid line) for 1801 UTC 27 Aug 92. Dashed line indicates virtual temperature of a parcel rising from 0.1 km AGL (~1000 mb)	32
8. RASS-derived virtual temperature profile (solid line) for 1831 UTC 27 Aug 92. Dashed line indicates virtual temperature of a parcel rising from 0.1 km AGL (~1000 mb)	32

9. RASS-derived virtual temperature profile (solid line) for 1901 UTC 27 Aug 92. Dashed line indicates virtual temperature of a parcel rising from 0.1 km AGL (~1000 mb)	33
10. RASS-derived virtual temperature profile (solid line) for 1931 UTC 27 Aug 92. Dashed line indicates virtual temperature of a parcel rising from 0.1 km AGL (~1000 mb)	33
11. RASS-derived virtual temperature profile (solid line) for 2001 UTC 27 Aug 92. Dashed line indicates virtual temperature of a parcel rising from 0.1 km AGL (~1000 mb)	34
12. RASS-derived virtual temperature profile (solid line) for 2031 UTC 27 Aug 92. Dashed line indicates virtual temperature of a parcel rising from 0.1 km AGL (~1000 mb)	34
13. RASS-derived virtual temperature profile (solid line) for 2101 UTC 27 Aug 92. Dashed line indicates virtual temperature of a parcel rising from 0.1 km AGL (~1000 mb)	35
14. RASS-derived virtual temperature profile (solid line) for 2131 UTC 27 Aug 92. Dashed line indicates virtual temperature of a parcel rising from 0.1 km AGL (~1000 mb)	35
15. RASS-derived virtual temperature profile (solid line) for 2201 UTC 27 Aug 92. Dashed line indicates virtual temperature of a parcel rising from 0.1 km AGL (~1000 mb)	36
16. RASS-derived virtual temperature profile (solid line) for 2231 UTC 27 Aug 92. Dashed line indicates virtual temperature of a parcel rising from 0.1 km AGL (~1000 mb)	36
17. RASS-derived virtual temperature profile (solid line) for 2301 UTC 27 Aug 92. Dashed line indicates virtual temperature of a parcel rising from 0.1 km AGL (~1000 mb)	37
18. RASS-derived virtual temperature profile (solid line) for 0001 UTC 28 Aug 92. Dashed line indicates virtual temperature of a parcel rising from 0.1 km AGL (~1000 mb)	37

19. West to east cross section through the first rainband of storm-relative helicity in the lowest 1.5 km AGL (solid line). Dashed line indicates the Davies-Jones et al. (1990) minimum threshold for mesocyclone development	42
20. West to east cross section through the second rainband of storm-relative helicity in the lowest 1.5 km AGL (solid line). Dashed line indicates the Davies-Jones et al. (1990) minimum threshold for mesocyclone development	43
21. East-west cross section (looking north) of convergence-induced vertical velocities in the first rainband. Speeds are in m/s and positive values indicate upward motions. 1.55 km depth ..	45
22. East-west cross section (looking north) of convergence-induced vertical velocities in the second rainband. Speeds are in m/s and positive values indicate upward motions. 1.55 km depth ..	46
23. East-west cross section (looking north) of convergence-induced vertical velocities in the first rainband. Speeds are in m/s and positive values indicate upward motions. 4.05 km depth ..	47
24. East-west cross section (looking north) of convergence-induced vertical velocities in the second rainband. Speeds are in m/s and positive values indicate upward motions. 4.05 km depth ..	48
25. East-west cross section (looking north) of the maximum CAPE-induced upward velocities in the first rainband. Speeds are in m/s	54
26. East-west cross section (looking north) of the maximum CAPE-induced upward velocities in the second rainband. Speeds are in m/s	55

LIST OF PLATES

PLATE	PAGE
I. Photograph of the Montgomery, AL Doppler radar taken at 1843 UTC 27 Aug 92. Image is folded or velocity-aliased and the elevation angle was 4.0°. Arrows indicate mesocyclone locations. Photograph by Walter Snell	20
II. Photograph of the Montgomery, AL Doppler radar taken at 1843 UTC 27 Aug 92. Image is unfolded or unaliased and the elevation angle was 4.0°. Arrows indicate mesocyclone locations. Photograph by Walter Snell	21
III. Photograph of the Montgomery, AL Doppler radar taken at 1907 UTC 27 Aug 92. Image is folded or velocity-aliased and the elevation angle was 0.0°. Photograph by Walter Snell	22

CHAPTER I

INTRODUCTION

Past studies of hurricane-induced tornadoes have dealt chiefly with the structure, thermodynamics, and dynamics of the parent tropical cyclone. There have been only a few observational studies of the tornadoes caused by hurricanes; all of which attempted to deduce the tornado's structure and characteristics without the benefit of Doppler radar. The consensus of these studies is that hurricane-induced tornadoes derive their circulations from the vertical tilting of horizontal vorticity created in the highly sheared environment of the landfalling hurricane. This research provides an analysis of the processes that led to the development of the tornadic, low-level circulations that occurred in Alabama and Georgia during the passage of Hurricane Andrew's remnants on 27 August 1992.

This thesis hypothesizes, given the low-level and shallow nature of the highly sheared layer, that boundary layer convergence zones, rather than convective updrafts, are the primary mechanism by which horizontal vorticity is turned vertical in the landfalling hurricane environment. Thus it follows that there will be more tornadoes spawned in hurricane

environments where boundary layer convergence boundaries or windshifts can exist.

Hurricane Andrew first made landfall near Homestead, Florida on 24 August 1992. After wreaking devastating damage on South Florida (but not inducing any confirmed tornadoes), it crossed the Gulf of Mexico and made final landfall in Louisiana on 26 August. Over the next three days as it recurved through the Southeastern and Mid-Atlantic states, Andrew and its extratropical remnants spawned 62 confirmed tornadoes (McCaul et al., 1993). This total is second only to Hurricane Beulah's 113 in 1967. As some of Andrew's rainbands and tornadic storms passed over the NWS Enterprise Doppler WSR-74C radar in Montgomery, Alabama and a 915 MHz profiler in western Georgia operated by the University of Alabama in Huntsville, data were collected that, as McCaul et al. put it, "offer what is believed to be the first chance to examine the structure of the tornado-bearing storms and rainbands as seen by such equipment." Also, a Radio Acoustic Sounding System (RASS) was attached to the profiler.

The literature on hurricane-tornadoes is somewhat limited and is reviewed in chapter II. There have been great volumes written, however, about the tornadoes of the central plains of the United States. These "Great Plains" tornadoes are often associated with a preceding mid-level mesocyclone in the parent storm. McCaul (1987) established the existence of such mesocyclonic circulations associated with the tornadoes

spawned by Hurricane Danny (1985). Wakimoto and Wilson (1989) called tornadoes associated with mesocyclones "supercell" tornadoes and those without mid-level rotations in the parent storms "non-supercell" tornadoes. Recent research of Great Plains tornadoes (Wilson et al., 1992; Wakimoto and Wilson, 1989; and Rotunno and Klemp, 1985) with mobile Doppler radars and numerical simulations indicates that upward-building low-level (below 2 km AGL) circulations may precede both supercell and non-supercell tornadoes. Given the subject of this thesis and the implication that low-level circulations may be a genesis mechanism and an early detection signature common to all tornadoes, some low-level rotation studies of Great Plains tornadoes are included in the review of chapter II.

Chapter III covers the methods to be used to collect and analyze the data for this study. Chapter IV will display and discuss the analyzed data in an effort to evaluate the hypotheses put forward in this section. Chapter V will provide a summary and conclusions to the thesis.

CHAPTER II

LITERATURE REVIEW

This chapter breaks the supporting literature for this project down into four subject areas: A) studies describing the structure and characteristics of hurricanes that spawn tornadoes, B) studies specifically describing the structure and characteristics of tornadoes spawned by hurricanes, C) applicable Great Plains tornado research, and D) summary and comments for the literature review. The third subject area presents recent general theory on Great Plains tornadogenesis, and then concentrates on research that emphasizes the importance of the low-level rotation.

A. Structure and Characteristics of Hurricanes that Spawn Tornadoes

This subject area includes the work of Smith (1965), Pearson and Sadowski (1965), Hill et al. (1966), Orton (1970), Fujita et al. (1972), Novlan and Gray (1974), Gentry (1983), and McCaul (1991). The literature before 1965 mainly documented the climatological aspects of hurricane-tornado outbreaks and the ideas presented are incorporated and updated in later works; consequently they are not covered here.

Smith (1965) and Hill et al. (1966) emphasized that hurricane-tornadoes mainly occur in the right-front quadrants (with respect to tropical storm motion) of hurricanes moving to the northeast. The data they had compiled up to that time clearly indicated that hurricanes recurving to the northeast had a higher probability of spawning tornadoes than those that continued westward. Hill et al. also stressed the importance of dry air intrusions at mid-levels as an important tornadogenetic factor. Recurvature and dry air intrusions are both indications that a tropical cyclone is falling under the influence of the westerlies and other extratropical effects (baroclinicity, cold air aloft, jet streaks, etc), and are reasonable causes given that they make the hurricane environment much more similar to the Great Plains environment that is most often associated with tornadoes.

In 1967 a northwestward moving tropical cyclone, Hurricane Beulah, slammed the Texas coast and then turned towards the southwest--producing at least 113 tornadoes in Texas alone. This clearly showed that recurvature to the northeast was not a necessary condition for hurricanes to produce tornadoes. Also, after the turn to the southwest, Beulah produced approximately one-third of its total tornadoes in the left-rear quadrant. Orton (1970), however, demonstrated that almost all Beulah's tornadoes occurred northeast of the hurricane center when the tornadoes were

plotted with respect to storm center and azimuth angle from true north.

Fujita et al. (1972) compiled a database of all the reported tornadoes occurring due to Japanese typhoons between 1950 and 1971. They noted a six-hour oscillation period for typhoon induced tornadoes and further noted a similar six-hour variation when applying a Fourier analysis to the hurricane-induced tornadoes studied by Hill et al. Little else has been published on this oscillation and it will not be further discussed here.

Novlan and Gray (1974) compiled a database for all U.S. hurricane spawned tornadoes occurring from 1948 to 1972. They collected "proximity" soundings for all tornado events and constructed composite hurricane centered plots of temperature and winds for various pressure levels for landfalling hurricanes with and without tornadoes. Their data compared favorably with that collected by Fujita et al. for Japanese typhoons. Novlan and Gray's composites allowed them to make comparisons to average hodographs of Great Plains tornadic storms; from this they determined that the chief similarity was the highly sheared layer between the surface and 1500 m (AGL). For hurricanes with tornadoes, this shear was strongest in the northeast quadrant and was mainly the result of a drastic drop in the composite wind speed from greater than 25 m s^{-1} at 850 mb to less than 10 m s^{-1} at the surface. For hurricanes without tornadoes the corresponding drop in

speed from 850 mb to the surface was 25 to 15 m s^{-1} . They proposed that the source of (vertical) vorticity for hurricane-tornadoes was the vertical tilting of the shear produced horizontal vorticity. Interestingly, Novlan and Gray attributed the greater shear in hurricanes with tornadoes to the faster filling rates of those tropical cyclones as opposed to the hurricanes without tornadoes. As they stated "hurricanes that fill the fastest develop the most intense cold-core structure and produce the largest vertical wind shear."

Gentry (1983) undertook a similar study to Novlan and Gray's and updated their database through 1982. He attributed the shear in the first 1500 m to the surface friction a hurricane encounters upon landfall. He argued that tornadogenesis within hurricanes generally occurs in the vicinity of airflow from the ocean to land (a large jump in surface friction) and that for hurricanes making landfall in the U.S., this usually means the right-front or northeast quadrant. Once the tropical cyclone moves inland, he mentioned that the filling mechanism noted by Novlan and Gray becomes important. Gentry also performed a scale analysis on the equation for vertical vorticity and showed, given the shear present in landfalling hurricanes, that the tilting term was at least two orders of magnitude larger than the others.

McCaul (1991) provides the most complete hurricane-tornado database to date, 1948 to 1986. His analysis

incorporates parameters such as convective available potential energy (CAPE), bulk Richardson number (BRN), BRN shear, helicity, and streamwise vorticity. He found lower-tropospheric vertical shears to be stronger in the hurricane-tornado environments than in the general Great Plains tornado composites. CAPE was determined to be far less than in the Great Plains cases, however he cautioned that low hurricane CAPE values are often related to their warmer anvil canopies aloft and should not be taken to mean a lack of instability in the lower troposphere (where the shear is at a maximum). McCaul also demonstrated that the lower-tropospheric shears and helicity are concentrated in the right-front quadrant of tornado producing hurricanes as a result of sheared steering currents. The right front quadrant was also associated with values of BRN in the "possible supercell" range. He further noted the number and intensity of hurricane-induced tornadoes increases for increasing hurricane intensity and size, that there is a preference for mid-afternoon occurrence, and that Gulf of Mexico tropical cyclones produce more tornadoes than their Atlantic counterparts.

B. Structure and Characteristics of Tornadoes Spawned by Hurricanes

As mentioned previously, there is a dearth of literature in this area. Rudd (1964) studied the tornadoes induced by Hurricane Carla (1961) and described highly tilted radar

echoes associated with some of the tornadic storms, perhaps indicating a highly sheared environment. Fujita et al. (1972) described damage caused by a multiple-vortex tornado in one of the typhoons they researched in Japan. Hoadley (1979) presented evidence of multiple vortices and a tornado-cyclone (mesocyclone producing a tornado) in the damage patterns of a tornado wrought by Hurricane David. Stiegler and Fujita (1982) surveyed the tornado damage caused by Hurricane Allen (1980) and reported that hurricane-tornadoes may reach F3 intensity. McCaul (1987) definitively documented mesocyclones (in the form of hook echoes and clearly photographed wall clouds with tornadoes) and supercell-like behavior in several of the tornado producing storms of Hurricane Danny's (1985) remnants. McCaul also observed that the "supercells" of Danny differed from their Great Plains counterparts in that they were significantly smaller and shallower and had relatively little heavy precipitation, hail, or lightning activity.

C. Applicable Great Plains Tornado Research

Due to the daunting amount of literature and often lengthy and involved explanations, only basic ideas of Great Plains tornadogenesis will be given here. This subject area includes the work of Leslie (1971), Smith and Leslie (1979), Rotunno and Klemp (1985), Davies-Jones (1986), Johnson et al. (1987), Wakimoto and Wilson (1989), Davies Jones et al. (1990), and Wilson et al. (1992).

Davies-Jones (1986) explained how a mid-level (2-5 km) cyclonic rotation (the mesocyclone) could develop in a thunderstorm given an environment of deeply sheared and veering winds. Smith and Leslie (1979) theoretically explained how under certain conditions the mesocyclone could interact with and build down towards the ground to produce a tornado. They argued that the updrafts that produce the mesocyclones have an hourglass shape with a minimum width (throat) at mid-levels owing to low-level convergence and upper-level divergence. Cyclostrophically, the strongest rotation and the lowest pressure is established at the throat. The pressure low at the throat impedes upward motion above it and increases upward flow below it. The increased flow from below enhances the rotation and establishes cyclostrophic balance at lower and lower levels. Therefore a strongly rotating cylinder of air (the mesocyclone) with limited entrainment through its sides builds downward towards the surface. Leslie (1971) pointed out that as the vortex begins to interact with the ground, its strength amplifies greatly because of retardation of the inflow and the resulting pressure fall.

Through a numerical simulation, Rotunno and Klemp (1985) showed that a mesocyclone and mesoanticyclone pair can develop in an updraft environment characterized by unidirectional shear. They also showed that the low-level circulation that presumably becomes the tornado may not be caused by forcing

from above; it may develop due to tilting by the updraft of solenoidally-produced horizontal vorticity along the outflow boundary (gust front) of the forward-flanking downdraft. Because its inflow is immediately restricted due to surface friction, the updraft can then rapidly stretch and concentrate this low-level circulation to exceed the mid-level rotation. Observational evidence from the Johnson et al. (1987) study strongly suggested that the low-level rotation is initiated by a separate mechanism than the mid-level rotation.

Wakimoto and Wilson (1989) and Wilson et al. (1992) examined the role of non-precipitation induced windshift lines in the initiation of convection and tornadogenesis. Wakimoto and Wilson showed that the windshift lines were often associated with shearing instabilities or eddies regardless of the lack of density or moisture contrasts across them (this is supported theoretically by Barcilon and Drazin, 1972). When convective updrafts later developed, these instabilities provided ambient vertical vorticity that could be stretched into non-supercell tornadoes. Wilson et al. demonstrated that vertical velocities along the windshift lines were maximized when the opposing wind components on either side of the line were nearly the same magnitude.

Wakimoto and Wilson speculated that a separately generated (or boundary layer forced) low-level rotation may be common to both supercell and non-supercell tornadoes; and that a superposition between the boundary layer forced low-level

rotation and the mid-level rotation may be necessary for devastating F3 to F5 tornadoes.

D. Summary and Comments for the Literature Review

Research on hurricane-tornadoes has made clear the importance of the highly sheared first 1500 m of landfalling tropical cyclones. It is presumed that it is the horizontal vorticity produced in this 1.5 km layer that is turned vertical to become the mesocyclone. Since the horizontal vorticity that becomes the mesocyclone circulation is confined near the surface, shear produced mesocyclones in the hurricane environment may not be mid-level circulations at all. In fact hurricane mesocyclones may be wholly within the boundary layer, and could be identified as the low-level rotation. Clearly, vertical motions within the boundary layer of landfalling tropical cyclones play a key role in the formation of the mesocyclones that precede the hurricane-spawned tornadoes.

CHAPTER III

METHODOLOGY

This chapter has three sections. The first describes what is needed to evaluate the hypothesis and identifies the key variables. The second section names the sources for the data. The third section briefly outlines the analysis methods.

A. What Is Needed

To evaluate the hypothesis that convergence lines provide more vertical tilting of vorticity than convective updrafts, the presence of low-level convergence boundaries must be shown to exist in the tornadic rainbands of Hurricane Andrew's remnants. It must be established that these convergence zones or boundaries produce vertical velocities in the lowest 1 to 2 km in excess of what would be permitted in light of convective available potential energy (CAPE). Furthermore, it must be demonstrated that small, low-level, vertically-oriented circulations (mesocyclones) preferentially form along these boundaries, and in some cases become tornado cyclones.

Key directly-measured variables for the analysis are virtual temperatures and horizontal wind speeds and directions

at specific heights above ground level (AGL). Important derived variables include CAPE, helicity, vorticity, vertical wind velocities, and saturated adiabatic lapse rates.

B. The Sources

There were two primary data sources for this work: the National Weather Service's (NWS) Enterprise Doppler WSR-74C radar in Montgomery, Alabama (MGM) and the University of Alabama in Huntsville's (UAH) 915 MHz profiler that was located in Carroll County, Georgia at the time of Hurricane Andrew's landfall. Other, secondary, sources included the U.S. Air Force Environmental Technical Applications Center (regional surface observations and rawinsonde data) and the Maxwell Air Force Base weather station (archived satellite images and regional radar summaries).

The Doppler radar in Montgomery is not equipped to electronically store any of the data or images which it displays. Therefore, data storage of images is usually accomplished by photographing the display console. Because it is not an automatic nor inexpensive procedure to photograph every radar image, photographic storage of data is generally only accomplished during periods of notable weather phenomena. The personnel at the NWS MGM site made the determination on 27 August 1992 that the passage of Hurricane Andrew's remnants constituted "notable" weather and photographs of the radar were taken at irregular intervals from 27/1243 to 27/1907 UTC.

The UAH profiler consists of a microwave radar component that measures a vertical profile of the wind vector and a Radio Acoustic Sounding System (RASS) component that measures virtual temperature profiles. On 27 August 1992 the profiler was deployed to the Wansley Power Plant site in Carroll County, Georgia (33.41N, 85.03W, elevation 222 m MSL). During Andrew's passage, the profiler was operated in both a "low" and a "high" mode. The low mode has a gate spacing and pulse length of 105 m, while the high mode has a gate spacing of 210 m and a pulse length of 420 m. Maximum sampling heights were approximately 4 and 7 km for the low and high modes, respectively. Three beams are used; one oriented vertically with the other two oriented 21° from vertical and arranged perpendicular to one another. Data provided by the profiler that are used in this study include signal-to-noise-ratios, hydrometeor fall speeds, and inferred horizontal winds. For the wind computations, it is assumed that each beam is sampling the same flow field and that the flow does not change significantly during the 105 s sampling cycle. Two researchers who have previously worked with the data presented in this thesis, Dr. Kevin Knupp (UAH) and Dr. Eugene McCaul (Universities Space Research Association, Hunstville), have gone to great lengths to ensure the data contained herein are essentially free of contamination by flow changes that might violate the above assumptions (McCaul et al., 1993).

The RASS utilizes 3 acoustic transducers, which surround the microwave antenna, and emit bursts of acoustic energy near 2 kHz frequency. These bursts produce fluctuations in density which travel upward at the speed of sound. The radar is then used to track the upward propagation speed of the acoustic or density disturbances. Since the speed of sound is directly proportional to the virtual temperature, a vertical profile of virtual temperature can be obtained. Maximum measuring heights are between 1 to 2 km and accuracy is approximately 1° C (Knupp, 1993).

C. Analysis Methods

To analyze the profiler data, the profiler's observations are plotted in vertical cross sections that employ a time-space technique (Fujita, 1963) to allow the observations from the single point to be spread out in a horizontal direction. Time-space plotting requires quantitative knowledge of the probed rainband motion; this is obtained from an analysis of several of the Doppler radar photographs.

Once the vertical cross sections of the profiler data are constructed, a two-dimensional mass continuity analysis of convergence and the resulting vertical velocities is undertaken. Also, two-dimensional analyses of helicity, CAPE, and vorticity are performed. Detailed explanations of these analyses are covered in section C of chapter IV.

CHAPTER IV

DATA AND ANALYSIS

This chapter is divided into four sections. Section A describes the meteorological event and how the data sources sampled that event. Section B documents observations of the data before analysis. Section C provides the analysis of the data, and Section D discusses the results of that analysis.

A. Hurricane Andrew

Figure 1 shows Hurricane Andrew's path and the locations of the tornadoes it spawned (indicated by F scale [Fujita 1973]) after it made landfall in Louisiana on 26 August 1992. By the time Andrew passed through Alabama and Georgia it had been downgraded to a tropical depression, but, according to Ostby and Weiss (1993), it still produced 13 tornadoes during that stage (27/0600 - 28/1200 UTC). Several of Andrew's rainbands swept through Alabama and Georgia on the afternoon and evening of the 27th. McCaul et al. (1993) describe the events as follows:

By midafternoon, Andrew's principle band had evolved into two nearly parallel lines of storms extending diagonally from northwest to southeast across Georgia, while a secondary band stretched almost north-south across eastern Alabama. The bands in Georgia fed into a curved arc of mostly stratiform rain in Tennessee, which could

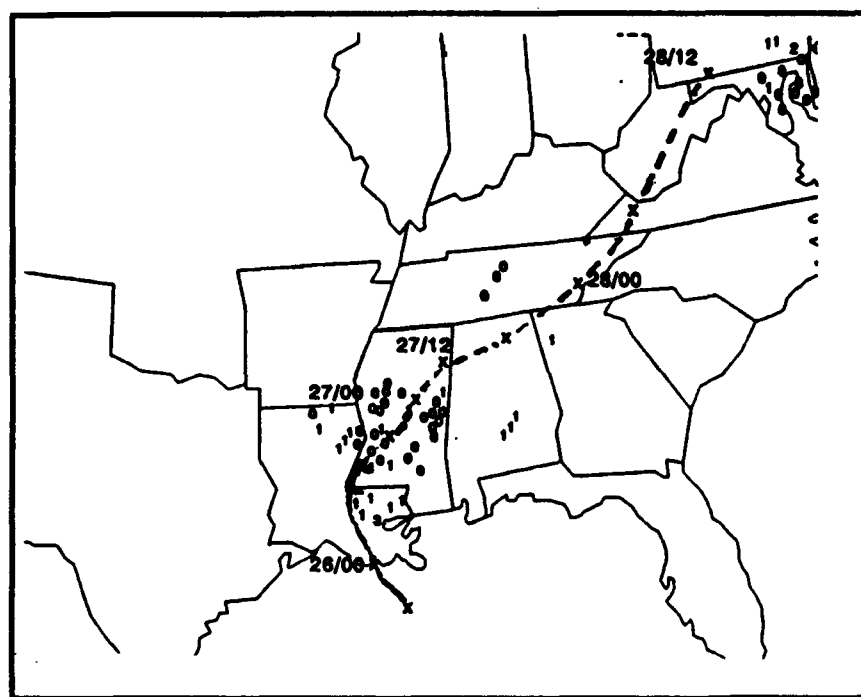


Figure 1. Track of Hurricane Andrew and associated tornadoes indicated by Fujita scale. From Ostby and Weiss (1993).

ultimately be traced back into Andrew's center in northwest Alabama. Andrew's precipitation shield was by this time fully asymmetrical, with very little rain southwest of the center. The bands generally had a cellular convective character in Georgia and southern Alabama, but were mostly stratiform in the region close to Andrew's center. Six of the seven confirmed tornadoes and all six funnel clouds reported within 5 h of 2030 UTC occurred in rainbands that were dominated by stratiform precipitation, but with embedded convection. Four confirmed tornadoes, including three near MGM and one near Rome, Georgia (RMG), can be attributed to the band that was in eastern Alabama at midafternoon.

Thus the same tornadic rainband that was interrogated by Doppler radar operators at MGM, was later probed by the UAH profiler and RASS in western Georgia. By day's end the UAH profiler had the opportunity to sample three of Andrew's rainbands, the second of which was the most severe (i.e. produced the tornadoes at MGM and RMG).

B. Observations of the Data

Plates I through III are photographs of the MGM Doppler radar display. Plate I was taken at 27/1843 UTC when the radar's antenna was positioned at an elevation angle of 4.0°; it is a folded (or velocity-aliased) image depicting the second (and the eastern edge of the third) of the three rainbands that moved through the MGM area on the 27th. During the period 27/1830-1930 UTC, three confirmed tornadoes occurred within 30 km of MGM (McCauley et al., 1993). At least two tornado cyclones (mesocyclones producing tornadoes) are evident in Plate I, one at azimuth 36° and range 20 km and the second at 132° and 12 km. Plate II is the same image as Plate

Plate I. Photograph of the Montgomery, AL Doppler radar taken at 1843 UTC 27 Aug 92. Image is folded or velocity-aliased and the elevation angle was 4.0°. Arrows indicate mesocyclone locations. Photograph by Walter Snell.



Plate II. Photograph of the Montgomery, AL Doppler radar taken at 1843 UTC 27 Aug 92. Image is unfolded or unaliased and the elevation angle was 4.0°. Arrows indicate mesocyclone locations. Photograph by Walter Snell.

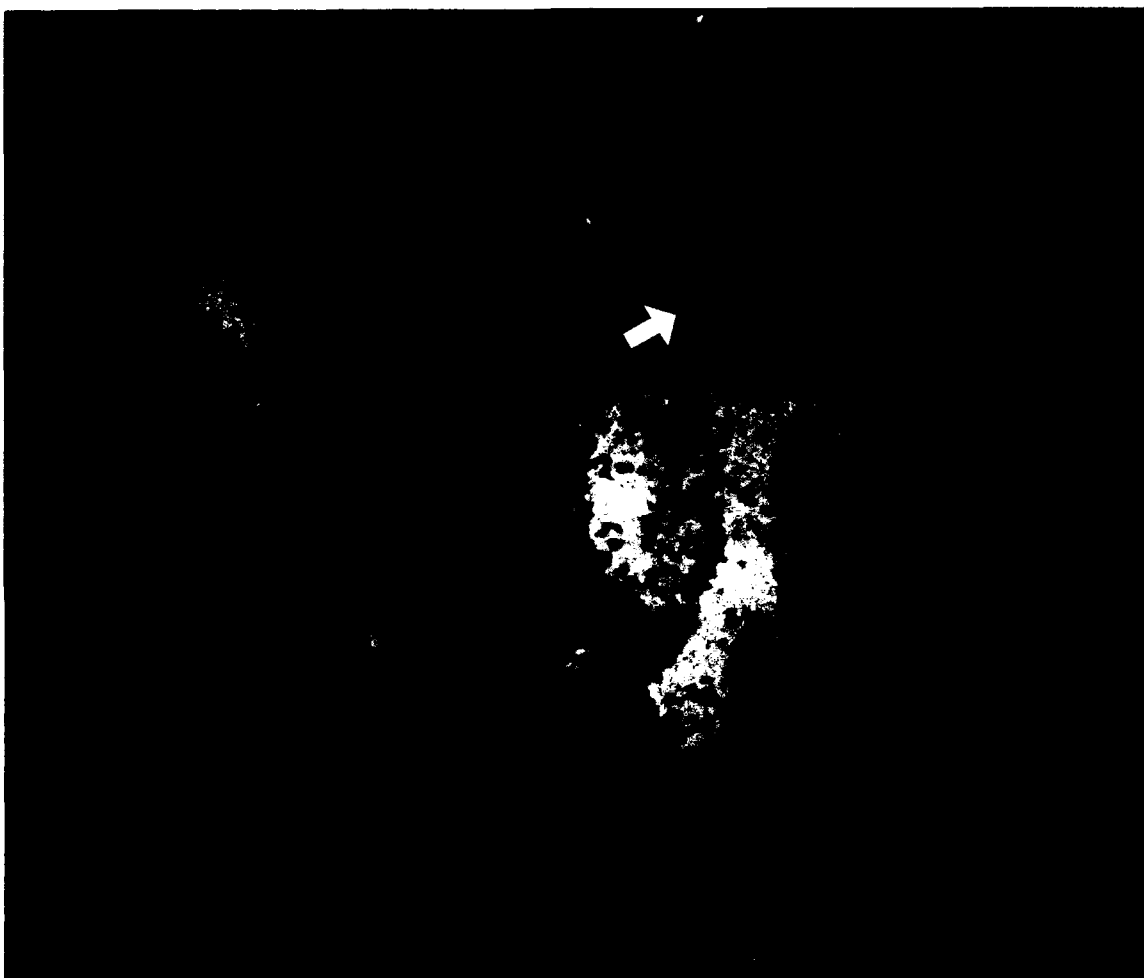


Plate III. Photograph of the Montgomery, AL Doppler radar taken at 1907 UTC 27 Aug 92. Image is folded or velocity-aliased and the elevation angle was 0.0°. Photograph by Walter Snell.



I, but unfolded (unaliased) using an algorithm built-in with the radar. Still evident in Plate II are the two tornado cyclones seen in Plate I; but even more noticeable is a snaking convergence boundary running approximately north-south through the MGM area. Both tornado cyclones appear to lie along this windshift line. Since at 4.0° elevation angle this windshift boundary becomes undiscernible beyond about 25 km, it appears to have been confined to below 1.8 km AGL. Using a subjective manual unfolding technique on an image similar to Plate I taken at 27/1839 UTC, McCaul et al. (1993) reported velocity convergence of up to 22 m s^{-1} across this boundary.

Plate III is another folded image taken at 27/1907 UTC. Because the elevation angle had been lowered to 0.0° , the convergence boundary is still apparent in Plate III even though it had moved so that much of it was approximately 40 km from the radar. Movement of the "S" curve feature (an undulation possibly caused by the southern tornado cyclone) from 27/1843 to 1907 UTC indicates a northeastward (from 225°) movement at 18.9 m s^{-1} for both the second rainband and its associated windshift.

Figure 2 is a time-height cross section of signal-to-noise ratio detected by the UAH profiler during the period 27/1645 to 28/0015 UTC. It distinctly shows the three rainbands that passed over the profiler; the boxed-in area represents the most severe area of the second band. Because the data were more complete for the first and second

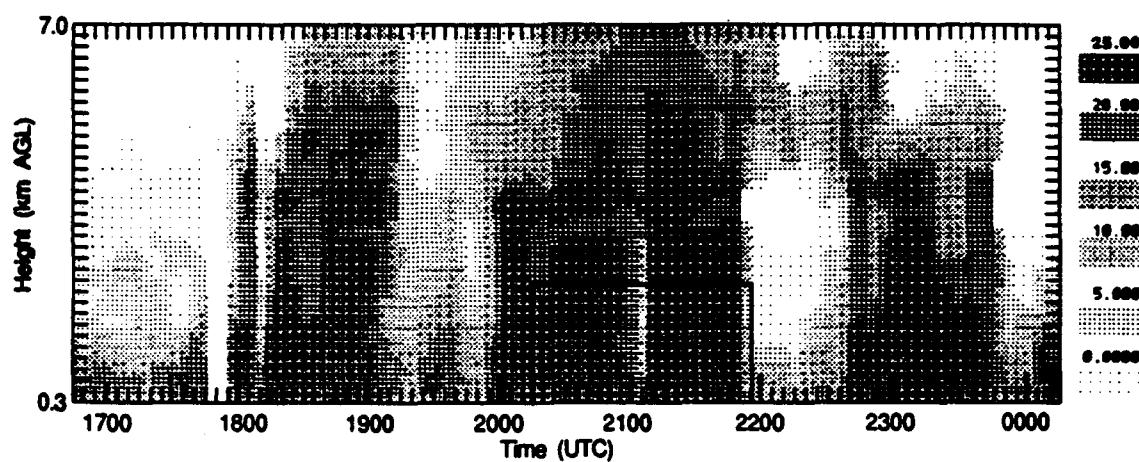


Figure 2. Time-height cross section of vertical beam signal-to-noise ratio (dB) for the period 1615 UTC 27 Aug to 0015 UTC 28 Aug 92. The boxed-in area indicates the encounter with the most severe section of the second rainband. From McCaul et al. (1993).

rainbands, the data fields for those two are analyzed in detail in this work while the third is not.

Figures 3 and 4 are time-height cross sections of the profiler measured horizontal winds in the central portions of the first and second rainbands respectively. Because there is profiler data from only one location, a time-space plotting procedure (Fujita, 1963) is used in Figures 3 and 4 and for all other plots and analyses in this work involving the profiler. Therefore, time progresses from right to left in Figures 3 and 4, and the spacing between the columns of winds is indicative of the amount of time that passes from column to column. Note the marked veering windshift between 27/2110 and 27/2114 UTC in the lowest kilometer of the second rainband (Figure 4); the fact that this feature becomes much less discernible above 1.1 km is in line with the observations of the MGM radar.

For the time-space plots and analyses that follow, an eastward (u-component) speed of 11.4 m s^{-1} was determined for the rainbands passing over the UAH profiler. Because the rainbands (and the windshift in the case of the second band) were oriented approximately north-south, the east-west horizontal axes of the plots are assumed normal the rainbands and associated windshifts. The u-component speed and the profiler sampling times were used to determine the distances that appear on the time-space plots and analyses. Distances increase towards the east and are measured from the windshifts

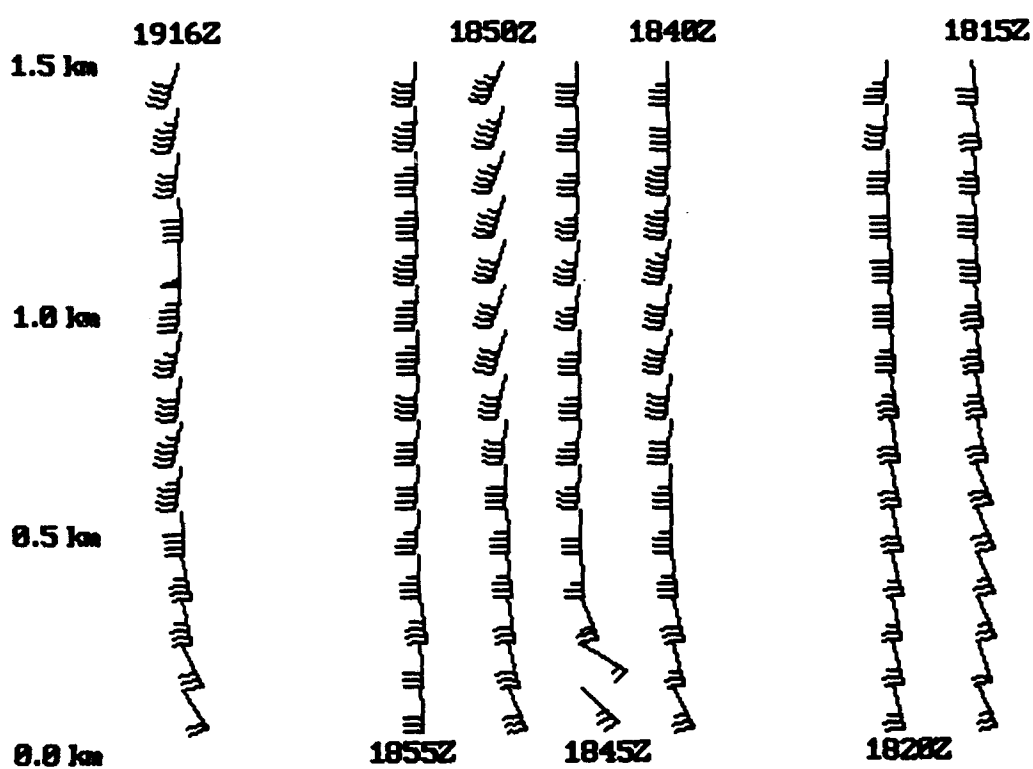


Figure 3. Time-height cross section of first rainband winds. Full barb indicates speeds of 5 m s^{-1} and half barb 2.5 m s^{-1} .

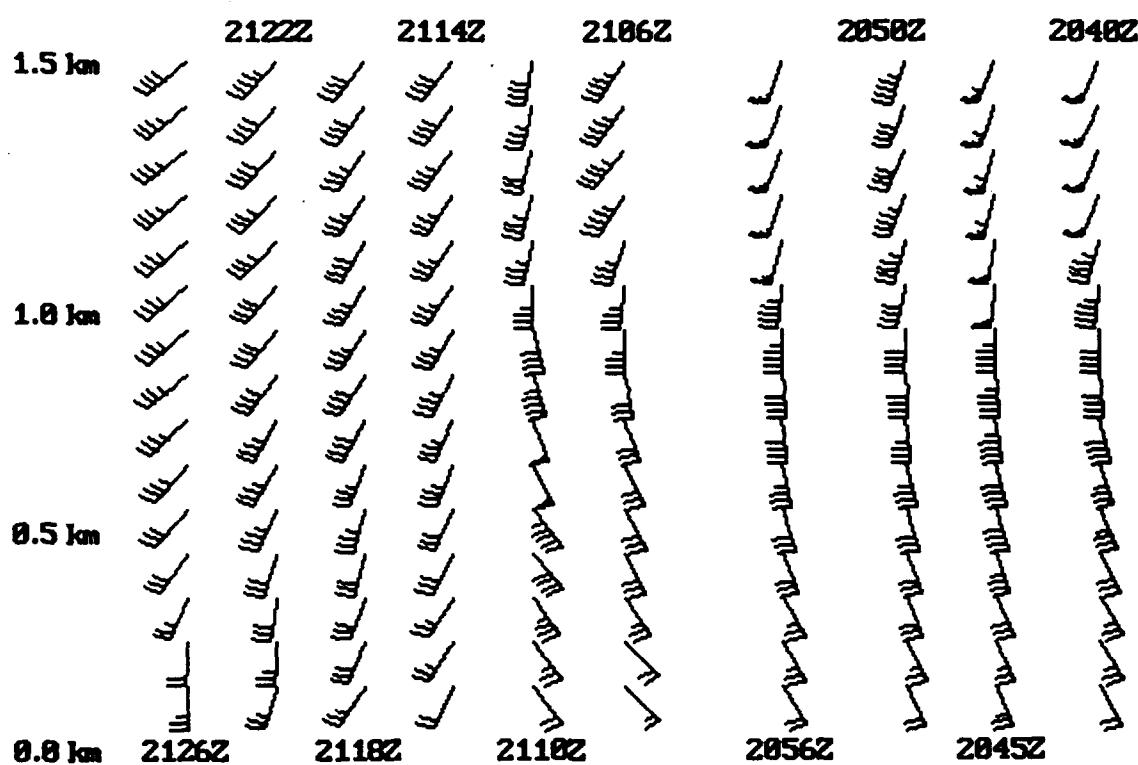


Figure 4. Time-height cross section of second rainband winds. Full barb indicates speeds of 5 m s^{-1} , half barb 2.5 m s^{-1} , and a pennant 25 m s^{-1} .

that appear in both rainbands. Windshift motion in all the time-space plots is to the right (east). The determination of the u-component speed will be discussed further in the next section.

Figures 5 and 6 are rainband cross sections (using the time-space method described above) depicting the hydrometeor fall speeds in the first and second bands respectively. Speeds are in m s^{-1} and are negative for downward motions. In both figures there appears to be an increase in fall speeds around the 4 km level. The 27/1200 UTC Centreville, AL (CKL) rawinsonde sounding (not shown) indicated that this level corresponded with the 0° C level, implying the increase in fall speeds to be attributable to a melting or bright band. Typical speeds above the melting level were approximately -1.5 m s^{-1} , while below it, as shown in Figures 5 and 6, speeds were generally -6 to -8 m s^{-1} . As McCaul et al. (1993) attested, both rainbands appear to have been almost exclusively stratiform in character. Of note, however, is the apparent disruption of the bright band in the second rainband (Figure 6) above the region of the windshift. This corresponds to the period 27/2110-2113 UTC when McCaul et al. (1993) claim the vertical velocity spectra (not analyzed in this study) "suggest the presence of a downshear tilted 5-10 m s^{-1} updraft centered near 2.5 km altitude, with some of the precipitation being carried upward." Figure 6 was constructed using "low" mode profiler data; data from the "high" mode at 27/2110 UTC

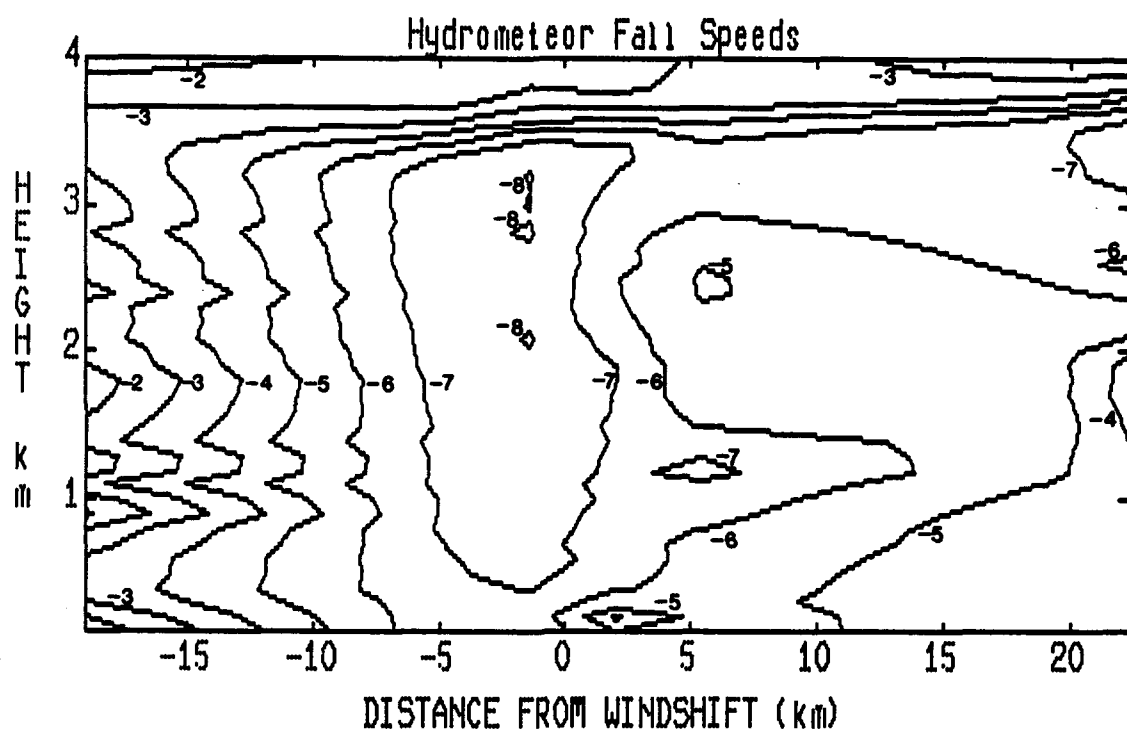


Figure 5. East-west cross section (looking north) of first rainband hydrometeor fall speeds. Speeds in m s^{-1} and negative values indicate downward motions.

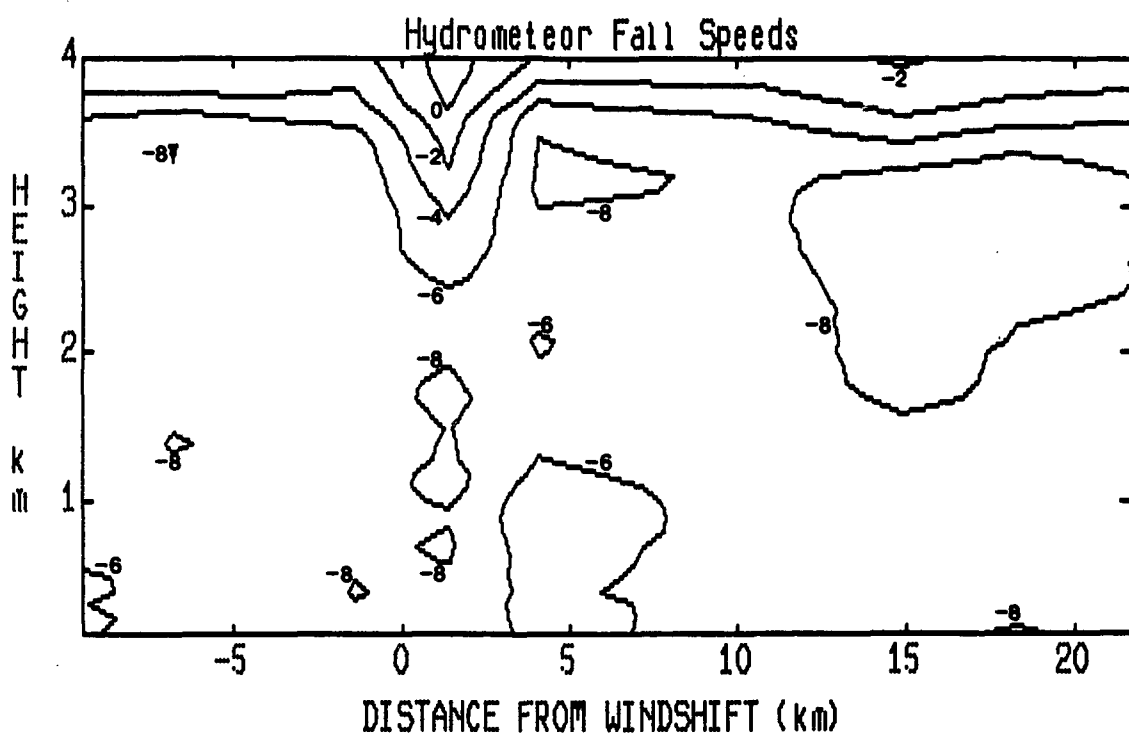


Figure 6. East-west cross section (looking north) of second rainband hydrometeor fall speeds. Speeds in m s^{-1} and negative values indicate downward motions.

show downward hydrometeor motion of only about -3 m s^{-1} between 1.7 and 4.0 km AGL--further suggesting an updraft occurred in this region.

The RASS data, sampled approximately every 100 m up to 2000 m every 30 minutes for the period 27/1801 - 28/0001 UTC, are shown plotted on the low-level skew-T/log p diagrams of Figures 7 through 18. The solid lines represent the virtual temperatures measured, and the dashed lines indicate the virtual temperature a saturated parcel rising from the 0.1 km level would have through the 0.1 to 2.0 km layer. For the purposes of reference, the 1000 mb level corresponds to about the 0.1 km level, 950 mb to 0.5 km, 900 mb to 1.0 km, 850 mb to 1.5 km, and 800 mb to 2.0 km. As can be quickly seen by looking over the skew-Ts, the virtual temperatures become somewhat erratic above 1.1 km (890 mb). For this reason analyses involving the RASS data were only performed up to the 1.1 km level. Based on the high signal-to-noise-ratios sensed in each of the three rainbands (indicating heavy precipitation) and the small or nonexistent dewpoint depressions recorded in the surface observations of sites affected by the rainbands, it is assumed that the environments shown in Figures 7-18 were saturated. This allows a determination of stability in the lowest 1.1 km (the boundary layer) for each time.

Instability below 1.1 km appears to have been present for at least the first (eastern) half of the first rainband

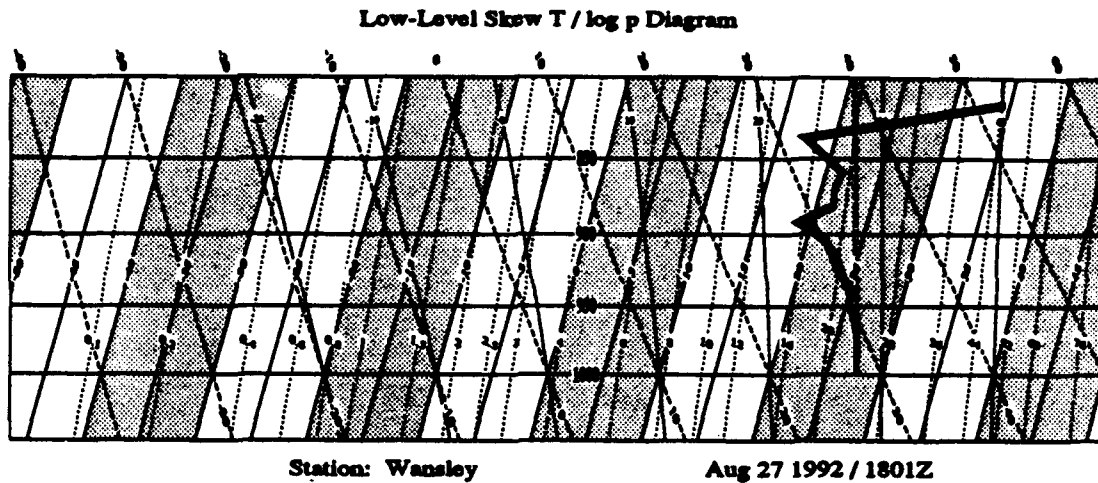


Figure 7. RASS-derived virtual temperature profile (solid line) for 1801 UTC 27 Aug 92. Dashed line indicates virtual temperature of a parcel rising from 0.1 km AGL (~1000 mb).

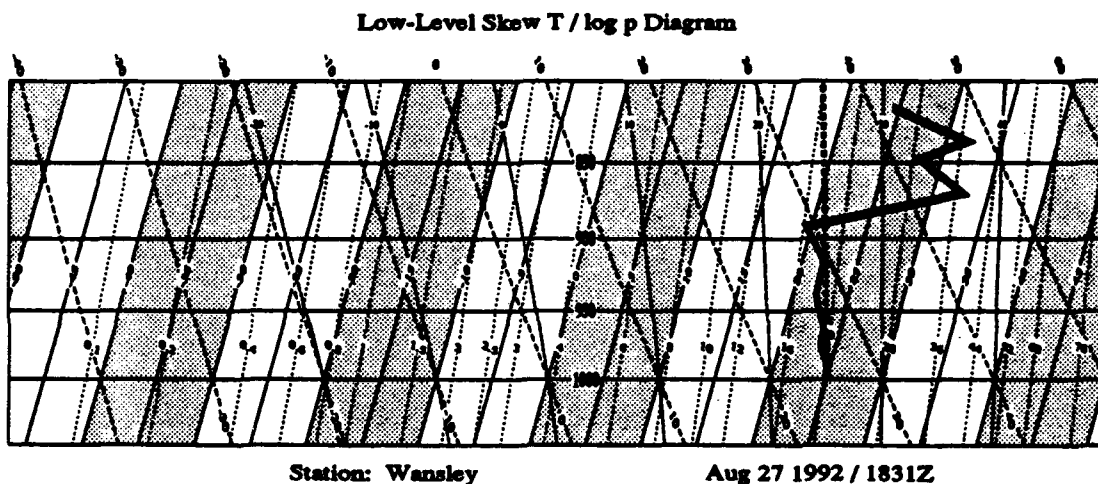


Figure 8. RASS-derived virtual temperature profile (solid line) for 1831 UTC 27 Aug 92. Dashed line indicates virtual temperature of a parcel rising from 0.1 km AGL (~1000 mb).

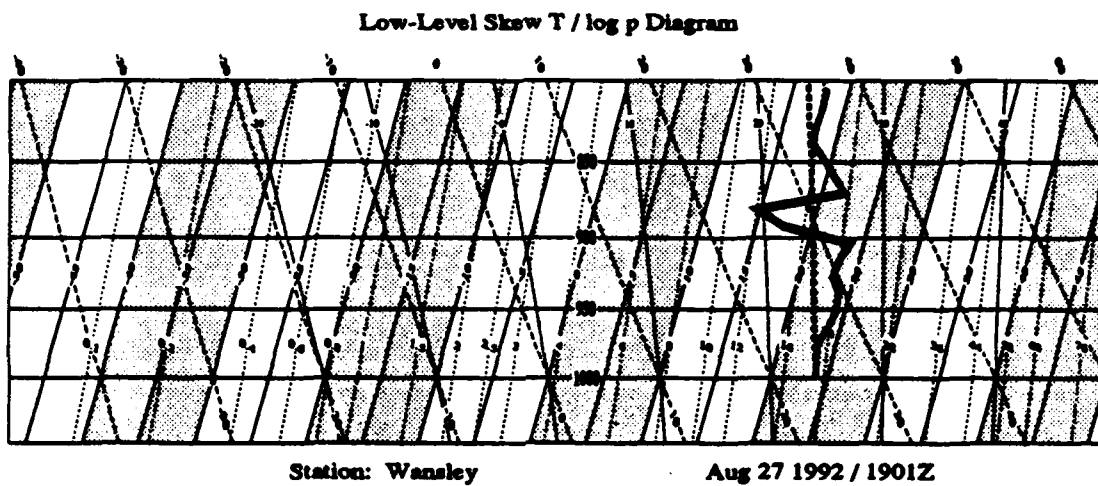


Figure 9. RASS-derived virtual temperature profile (solid line) for 1901 UTC 27 Aug 92. Dashed line indicates virtual temperature of a parcel rising from 0.1 km AGL (~1000 mb).

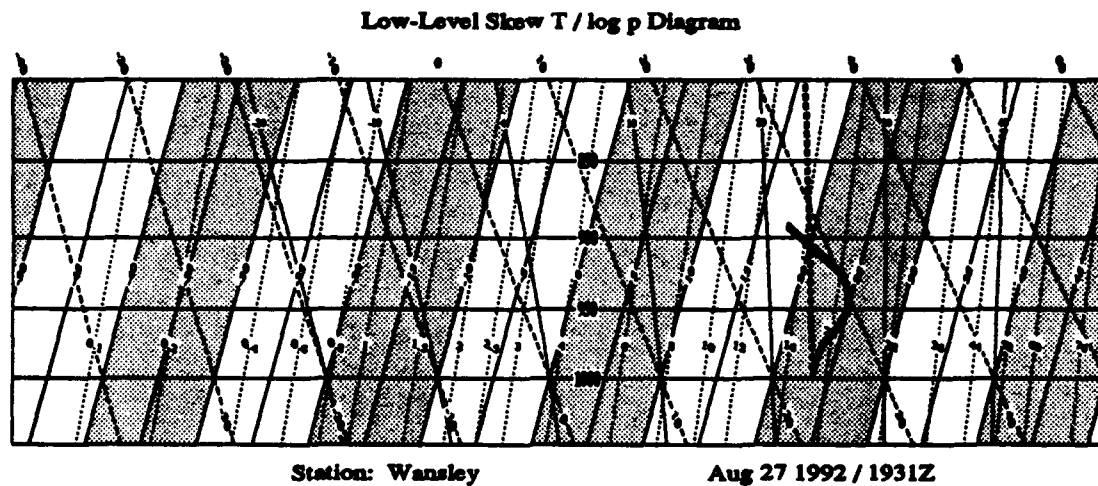


Figure 10. RASS-derived virtual temperature profile (solid line) for 1931 UTC 27 Aug 92. Dashed line indicates virtual temperature of a parcel rising from 0.1 km AGL (~1000 mb).

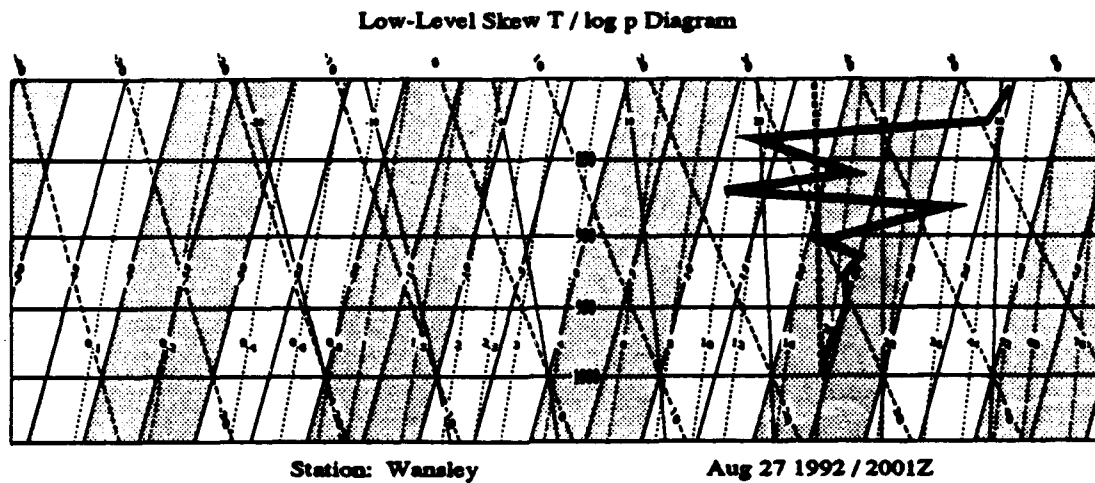


Figure 11. RASS-derived virtual temperature profile (solid line) for 2001 UTC 27 Aug 92. Dashed line indicates virtual temperature of a parcel rising from 0.1 km AGL (~1000 mb).

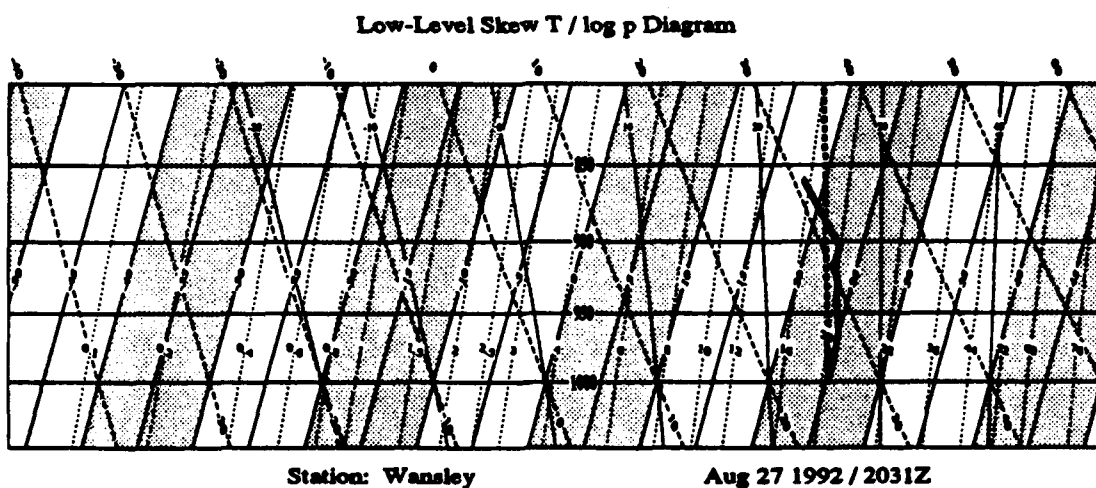


Figure 12. RASS-derived virtual temperature profile (solid line) for 2031 UTC 27 Aug 92. Dashed line indicates virtual temperature of a parcel rising from 0.1 km AGL (~1000 mb).

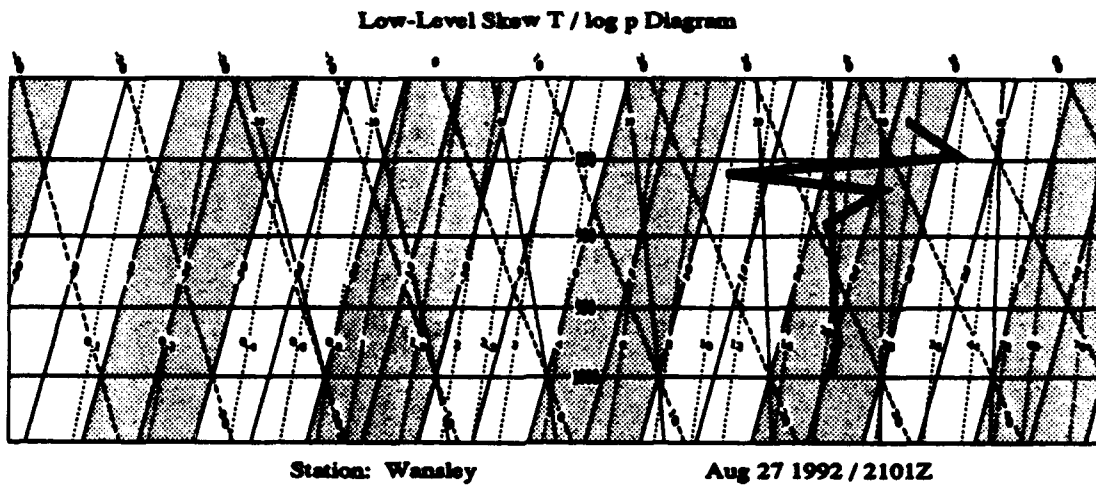


Figure 13. RASS-derived virtual temperature profile (solid line) for 2101 UTC 27 Aug 92. Dashed line indicates virtual temperature of a parcel rising from 0.1 km AGL (~1000 mb).

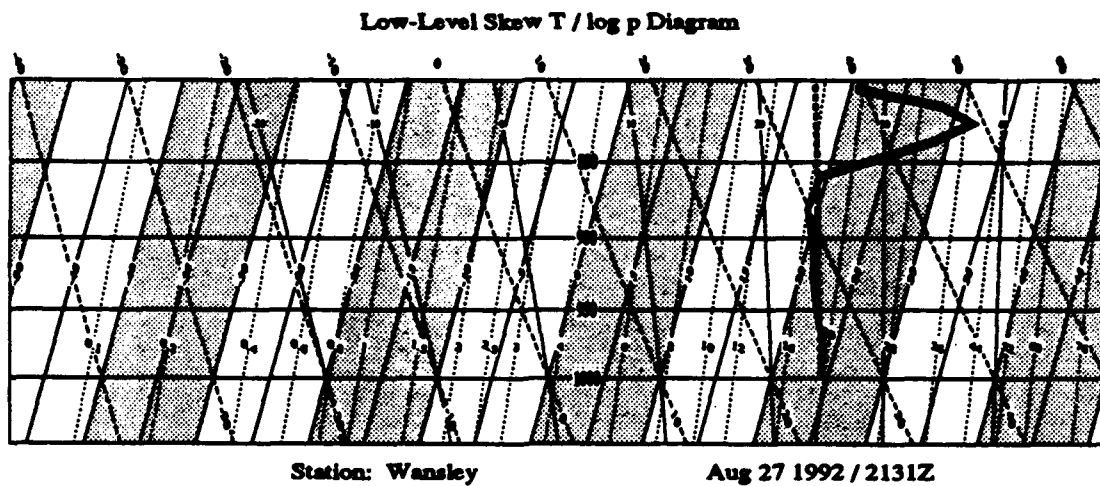


Figure 14. RASS-derived virtual temperature profile (solid line) for 2131 UTC 27 Aug 92. Dashed line indicates virtual temperature of a parcel rising from 0.1 km AGL (~1000 mb).

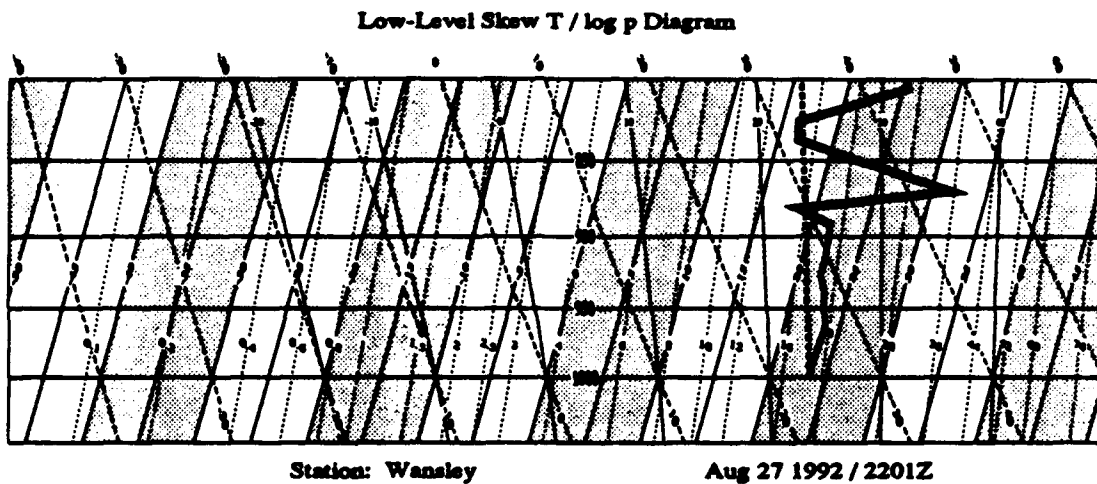


Figure 15. RASS-derived virtual temperature profile (solid line) for 2201 UTC 27 Aug 92. Dashed line indicates virtual temperature of a parcel rising from 0.1 km AGL (~1000 mb).

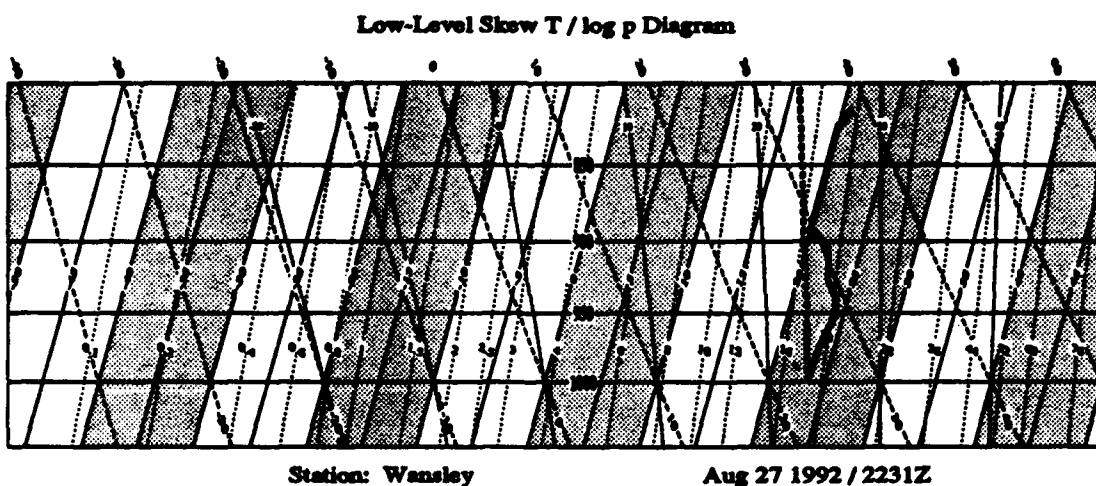


Figure 16. RASS-derived virtual temperature profile (solid line) for 2231 UTC 27 Aug 92. Dashed line indicates virtual temperature of a parcel rising from 0.1 km AGL (~1000 mb).

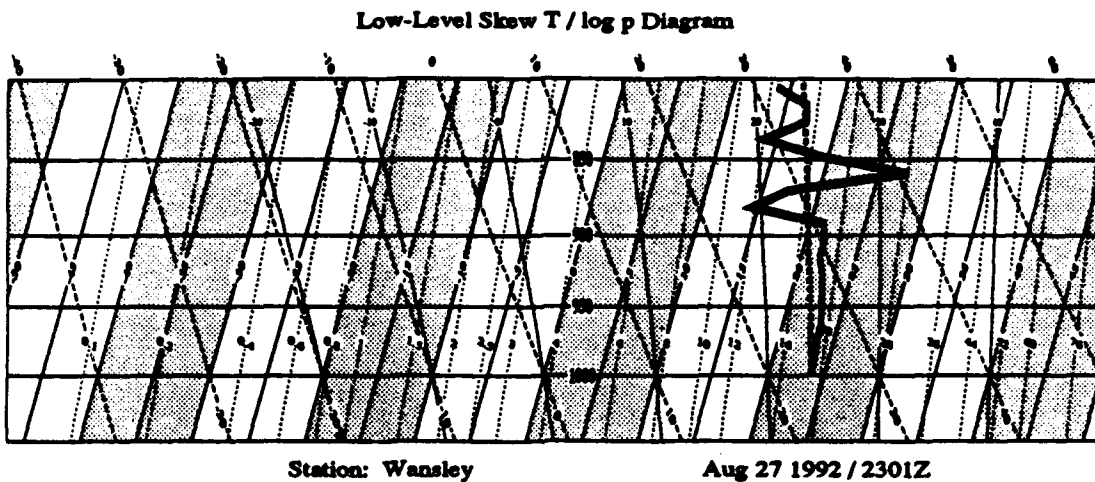


Figure 17. RASS-derived virtual temperature profile (solid line) for 2301 UTC 27 Aug 92. Dashed line indicates virtual temperature of a parcel rising from 0.1 km AGL (~1000 mb).

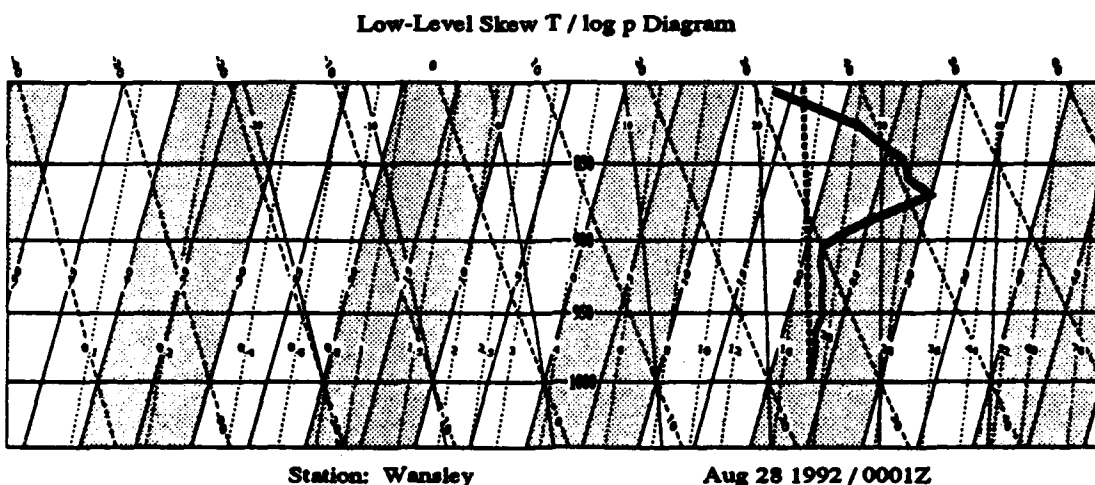


Figure 18. RASS-derived virtual temperature profile (solid line) for 0001 UTC 28 Aug 92. Dashed line indicates virtual temperature of a parcel rising from 0.1 km AGL (~1000 mb).

(Figures 7 and 8). Boundary layer instability for this region and time is in line with GOES satellite imagery (not shown) from 27/1731 - 1801 UTC which indicated an area of markedly reduced cloudiness just ahead of the first rainband in western Georgia. The boundary layer remained remarkably stable or neutral through most of the second rainband's passage; Figure 14 shows the slight instability that developed toward the rear (western-most) portion of the rainband. The boundary layer of the third rainband was stable throughout its passage over the RASS.

It should be noted that the profiler winds and RASS soundings recorded between 27/2030 - 2130 UTC qualify as tornado "general" proximity soundings (within 3 h and 185 km), as defined by Novlan and Gray (1974) and carried on by McCaul (1991), for both the MGM and RMG tornadoes. These data nearly meet McCaul's (1991) qualifications of within 2 h and 40 km for "close" proximity soundings for the RMG tornado (RMG is approximately 80 km from the profiler site).

C. Analysis

The goal of this section is three-fold. First, it must be established that wind shears favorable for tornadogenesis were present in the lowest 1500 m of the tornado-producing second rainband that passed over MGM and the UAH profiler. Second, it must be shown that the vertical velocities necessary to take advantage of the favorable shears could be

produced by mass convergence at the windshift boundary. Third, it must be demonstrated that any upward buoyant motions within the boundary layer did not coincide with the location(s) of tornadogenesis.

Before going any further, the determination of rainband motion at the profiler site must be explained. The velocity of propagation reflects a blending of the second rainband motion as deduced from measurements of the MGM radar photographs with the motion of Andrew's center as determined by the National Hurricane Center (NHC). From Figure 1 (NHC's best track data for Andrew provided to Ostby and Weiss [1993] by Ed Rappaport), it appears Andrew's center was moving eastward (u-component) at about 9.4 m s^{-1} during the period 27/1800 - 28/0000 UTC. The MGM radar photographs indicate an eastward (u-component) movement of the second rainband at about 13.4 m s^{-1} . It is assumed that the rainbands under consideration here lay approximately along longitude lines and remained that way as they moved northeastward with Andrew's center between 27/1800 and 28/0000 UTC. To do so, the southern portions of the rainbands had to move slightly faster to the east than the northern portions because of the spherical nature of the earth. Because the UAH profiler site was approximately half way between the latitude of MGM and the latitude of Andrew's center during 27/1800 - 28/0000 UTC, an average u-component of 11.4 m s^{-1} was assigned to the rainbands at the profiler site. Andrew's northward (v-component)

movement was only 4.0 m s^{-1} at this time. Based on the center's slower progression northwards than the 13.4 m s^{-1} for the second rainband at MGM, and regional radar reports that indicated that the rainbands were moving in the same direction in western Georgia as they had been in Alabama, a v-component of 11.4 m s^{-1} was given to the rainbands at the profiler site.

Given a rainband movement from 225° at 16.1 m s^{-1} , storm-relative helicity computations can be made on the profiler data for the first and second rainbands. Davies-Jones et al. (1990) showed storm-relative helicity to be a useful forecast tool for measuring the properties of the low-level wind shear associated with the development of mesocyclone-induced tornadoes. Based on a study of tornado proximity soundings for 28 tornado cases, Davies-Jones et al. determined approximate ranges of helicities for three categories of tornado intensity: weak (F0, F1), strong (F2, F3), and violent (F4, F5) on the F0-F5 Fujita tornado intensity scale. The three ranges of helicity values correspond to $150-299 \text{ J kg}^{-1}$ (weak), $300-449 \text{ J kg}^{-1}$ (strong), and $\geq 450 \text{ J kg}^{-1}$ (violent).

As has been noted by several researchers--McCaull (1991), Gentry (1983), and Novlan and Gray (1974) to name a few--and is quite evident in the profiler data of Figures 3 and 4, the veering and speed shear that often characterizes hurricane-tornado environments occurs almost exclusively below 1.5 km AGL. In light of this, the storm-relative helicity calculations performed in this work are confined to this

layer. Storm-relative helicity is calculated by first determining the total helicity (Lilly, 1986):

$$\begin{aligned} H_{\text{Tot}} &= (V - V_s) \cdot (k \times \partial V / \partial z) \\ &= (v - v_s) \partial u / \partial z - (u - u_s) \partial v / \partial z \end{aligned} \quad (1)$$

where V = the layer average wind
(with u - and v -components)
 V_s = storm motion
(with u_s - and v_s -components)

and then multiplying by the depth of the averaging layer. Storm-relative helicity was determined for each column that appears in Figures 3 and 4. To reduce sensitivity to small scale wind variations, the average u - and v -components were determined for the 100-500 m layer, the 1000-1500 m layer, and for the entire 1500 m layer for each column. The u and v differences between the 100-500 m layer and the 1000-1500 m layer determined the values of $\partial u / \partial z$ and $\partial v / \partial z$. The values for storm movement, u_s and v_s , were assumed to be the same as for the rainband movement. The values of the 0-1.5 km storm-relative helicity are displayed for the first and second rainbands in Figures 19 and 20, respectively. Note that in advance of the second rainband windshift the helicity values exceed the Davies-Jones et al. threshold by approximately 33%.

To determine the vertical velocities created by mass convergence, the incompressible continuity equation,

$$\partial w / \partial z = -(\partial u / \partial x + \partial v / \partial y) \quad (2)$$

where w = the vertical wind component

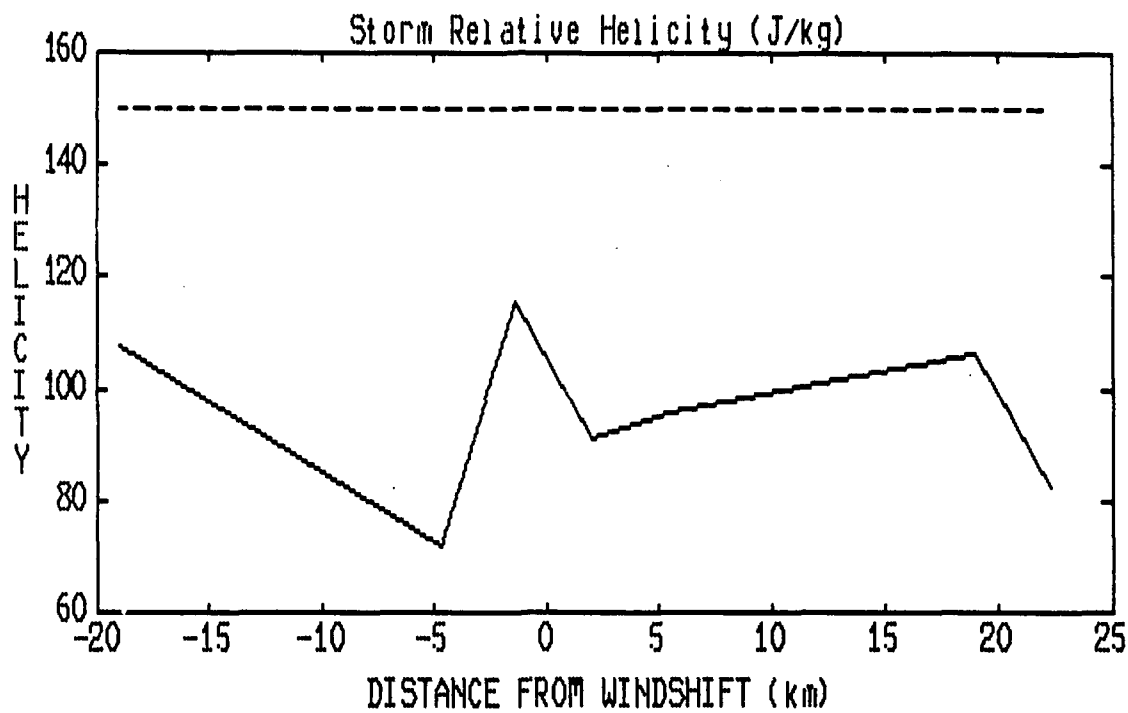


Figure 19. West to east cross section through the first rainband of storm-relative helicity in the lowest 1.5 km AGL (solid line). Dashed line indicates the Davies-Jones et al. (1990) minimum threshold for mesocyclone development.

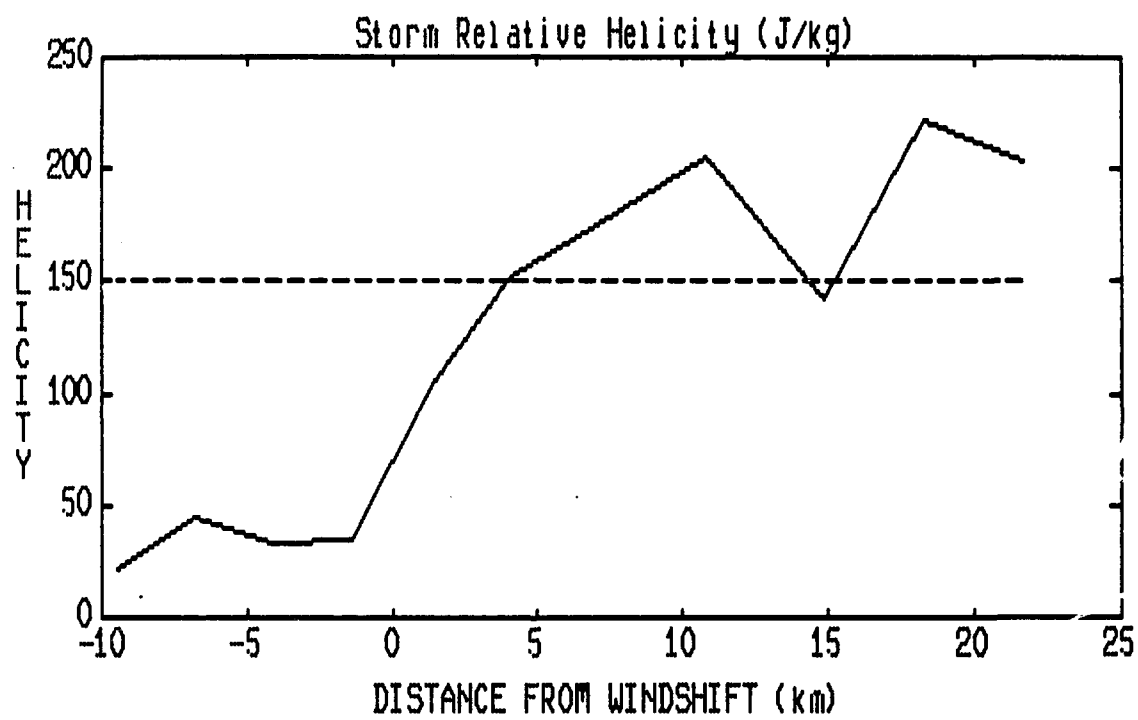


Figure 20. West to east cross section through the second rainband of storm-relative helicity in the lowest 1.5 km AGL (solid line). Dashed line indicates the Davies-Jones et al. (1990) minimum threshold for mesocyclone development.

was applied to the regions between the columns of winds in each rainband. Since the rainbands and their windshifts were assumed to be running north-south, without north-south variation, the $\partial v / \partial y$ term disappears. Integrating (2) without $\partial v / \partial y$ from the top of a given layer (z_2) to the bottom (z_1) yields

$$\begin{aligned} w(z_2) &= -(\partial u / \partial x)_{\text{ave}}[z_2 - z_1] + w(z_1) \\ &\approx -[(u_2 - u_1)/(x_2 - x_1)][z_2 - z_1] + w(z_1) \quad (3) \end{aligned}$$

Assuming the horizontal wind shear, $\partial u / \partial x$, is the average for the 100 m layer that runs from 50 m below the wind difference to 50 m above it, and adding all those layers together up to the 1.55 km level, produces the vertical velocity plots seen in Figures 21 (first rainband) and 22 (second rainband). Figures 23 and 24 are the same as 21 and 22 except they extend up to the 4.05 km level. Note the $>5 \text{ m s}^{-1}$ updraft that appears at the windshift in both Figures 22 and 24.

As a check of the incompressible assumption, the RASS derived virtual temperatures can be used to allow boundary layer density variations to be incorporated with the profiler winds when making continuity computations. Starting with the mass divergence form of the continuity equation,

$$\partial \rho / \partial t = -[\partial(\rho u) / \partial x + \partial(\rho v) / \partial y + \partial(\rho w) / \partial z] \quad (4)$$

where ρ = density

and eliminating the north-south component while solving for

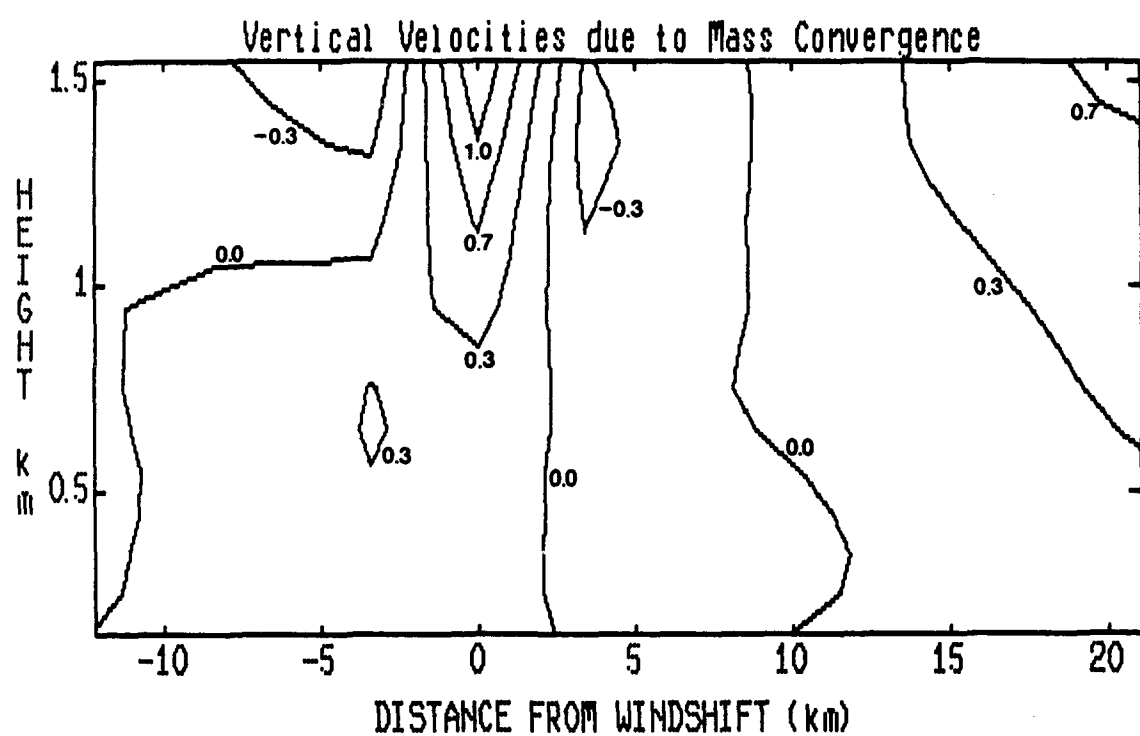


Figure 21. East-west cross section (looking north) of convergence-induced vertical velocities in the first rainband. Speeds are in m s^{-1} and positive values indicate upward motions. 1.55 km depth.

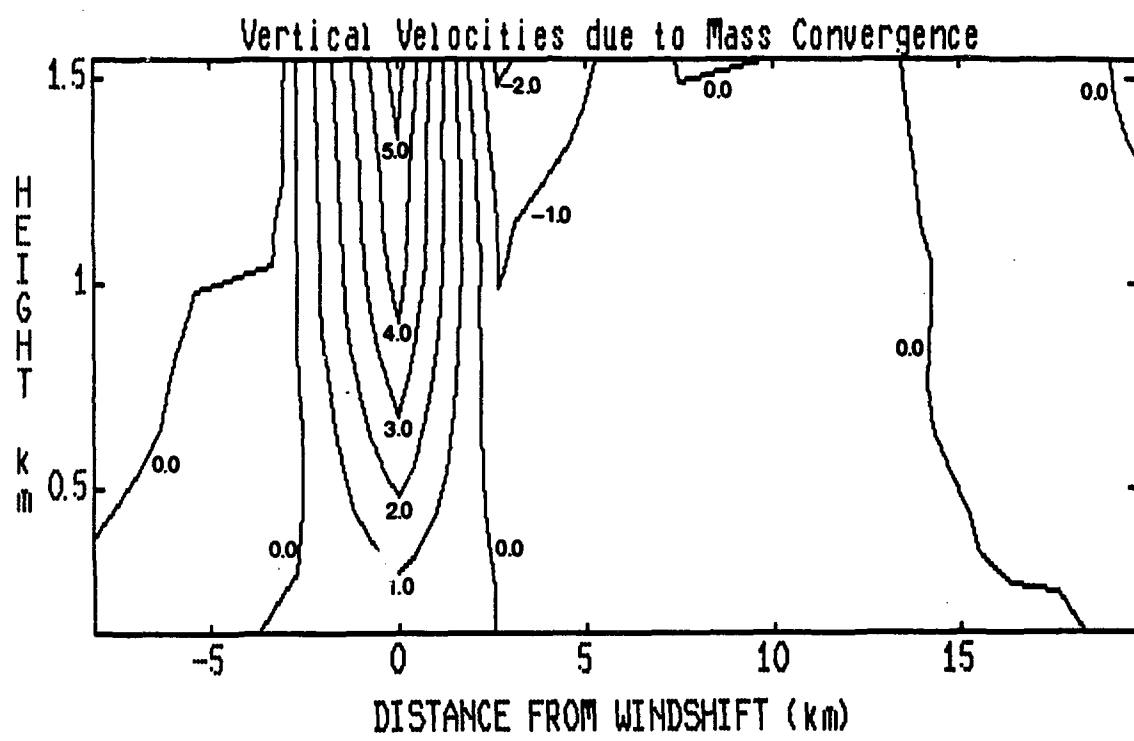


Figure 22. East-west cross section (looking north) of convergence-induced vertical velocities in the second rainband. Speeds are in m s^{-1} and positive values indicate upward motions. 1.55 km depth.

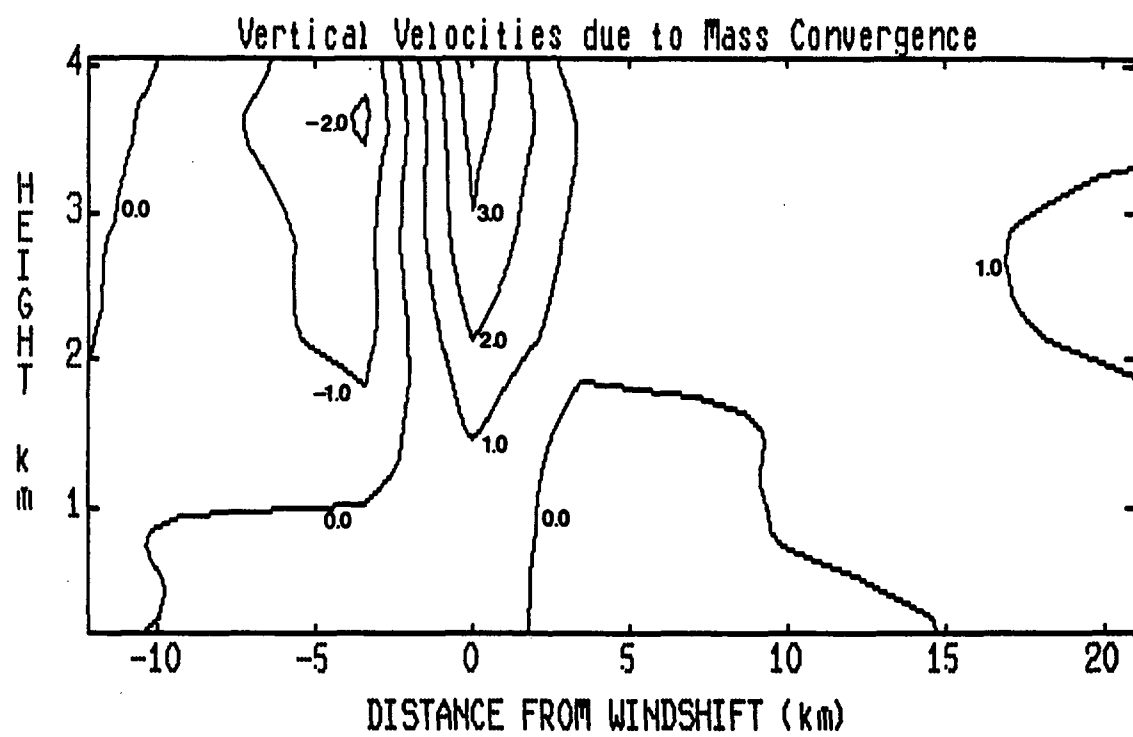


Figure 23. East-west cross section (looking north) of convergence-induced vertical velocities in the first rainband. Speeds are in m s^{-1} and positive values indicate upward motions. 4.05 km depth.

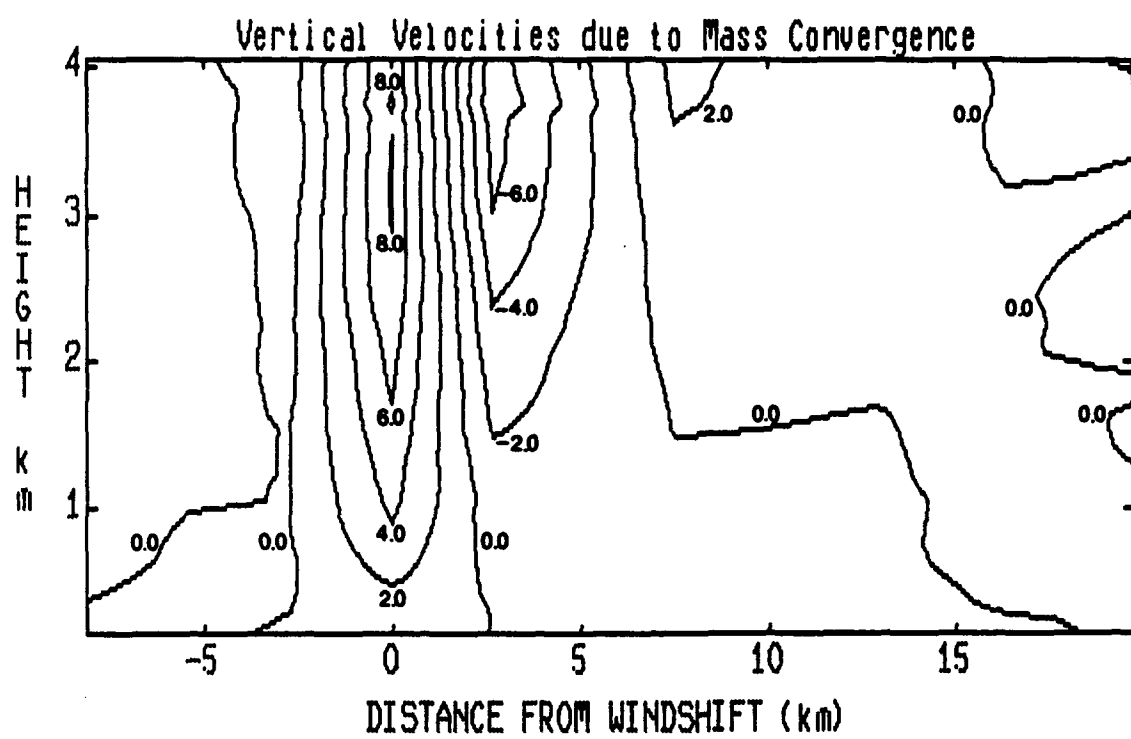


Figure 24. East-west cross section (looking north) of convergence-induced vertical velocities in the second rainband. Speeds are in m s^{-1} and positive values indicate upward motions. 4.05 km depth.

the vertical component yields,

$$\frac{\partial(\rho w)}{\partial z} = -[\frac{\partial(\rho u)}{\partial x} + \frac{\partial \rho}{\partial t}] \quad (5)$$

Integrating as before and solving for $w(z_2)$ produces a similar equation to (3),

$$w(z_2) \approx (\rho_{z_1}/\rho_{z_2})w(z_1) - [(\frac{z_2 - z_1}{\rho_{z_2}})[(\rho_2 u_2 - \rho_1 u_1)/(x_2 - x_1) + (\rho_2 - \rho_1)/(t_2 - t_1)] \quad (6)$$

where ρ_{z_2} and ρ_{z_1} = the densities at z_2 and z_1 , respectively
 ρ_2 and ρ_1 = the densities at x_2 and x_1 , respectively

but (6) allows for both vertical and horizontal density variations. Since the RASS virtual temperatures were sampled only every half-hour, a linear interpolation was performed on the data to permit a virtual temperature profile to be assigned to each time column in each rainband. Densities were obtained from the virtual temperatures using the equation of state, $\rho = p/(R_d T_v)$, where R_d is the ideal gas constant for dry air and T_v is the virtual temperature. Pressures for each layer were calculated from the Standard Atmosphere equations in the Smithsonian Meteorological Tables (List, 1984). Because (6) requires density differences both vertically and horizontally, calculation layers in this case ran from 100-200 m, 200-300 m, and so forth up to the 1000-1100 m layer. The u-component wind differences were averages for the layer. Tables 1 (first rainband) and 2 (second rainband) compare the values of vertical velocity derived using the different

Table 1. First rainband height vs. time values of vertical velocity calculated assuming an incompressible atmosphere (top) and calculated allowing RASS-derived density variations (bottom). Speeds are in m s^{-1} and positive values indicate upward motions.

VERTICAL VELOCITIES (m/s) -- INCOMPRESSIBLE ATMOSPHERE

	1906Z	1853Z	1848Z	1843Z	1830Z	1817Z
1.55 km	-0.04	-0.61	1.13	-0.34	0.18	0.67
1.45 km	-0.06	-0.48	0.97	-0.38	0.19	0.60
1.35 km	-0.07	-0.37	0.83	-0.40	0.21	0.49
1.25 km	-0.07	-0.23	0.68	-0.37	0.20	0.44
1.15 km	-0.06	-0.11	0.57	-0.33	0.18	0.40
1.05 km	-0.05	-0.01	0.47	-0.30	0.15	0.37
0.95 km	-0.05	0.10	0.37	-0.26	0.12	0.34
0.85 km	-0.06	0.21	0.25	-0.18	0.08	0.33
0.75 km	-0.07	0.26	0.17	-0.13	0.05	0.31
0.65 km	-0.08	0.27	0.16	-0.12	0.02	0.28
0.55 km	-0.09	0.25	0.18	-0.16	0.00	0.23
0.45 km	-0.08	0.20	0.21	-0.18	-0.02	0.16
0.35 km	-0.06	0.16	0.24	-0.21	-0.03	0.12
0.25 km	-0.06	0.16	0.20	-0.19	-0.02	0.06
0.15 km	-0.03	0.11	0.09	-0.08	-0.02	0.04

VERTICAL VELOCITIES (m/s) -- ALLOWING DENSITY VARIATIONS

	1906Z	1853Z	1848Z	1843Z	1830Z	1817Z
1.1 km	-0.05	-0.10	0.49	-0.29	0.18	0.39
1.0 km	-0.04	0.00	0.39	-0.25	0.15	0.36
0.9 km	-0.05	0.11	0.28	-0.19	0.11	0.33
0.8 km	-0.06	0.19	0.18	-0.12	0.08	0.31
0.7 km	-0.06	0.22	0.13	-0.09	0.04	0.28
0.6 km	-0.08	0.22	0.13	-0.11	0.02	0.24
0.5 km	-0.07	0.18	0.16	-0.13	0.00	0.18
0.4 km	-0.06	0.13	0.19	-0.15	-0.01	0.12
0.3 km	-0.04	0.11	0.18	-0.16	-0.01	0.07
0.2 km	-0.03	0.08	0.10	-0.09	-0.01	0.03

Table 2. Second rainband height vs. time values of vertical velocity calculated assuming an incompressible atmosphere (top) and calculated allowing RASS-derived density variations (bottom). Speeds are in m s^{-1} and positive values indicate upward motions.

VERTICAL VELOCITIES (m/s) -- INCOMPRESSIBLE ATMOSPHERE

	2124Z	2120Z	2116Z	2112Z	2108Z	2101Z	2053Z	2048Z	2043Z
1.55 km	1.00	0.52	-0.06	5.50	-2.18	0.03	-0.04	0.22	-0.06
1.45 km	0.95	0.44	-0.06	5.23	-1.90	-0.02	-0.06	0.27	-0.06
1.35 km	0.90	0.35	-0.05	4.98	-1.62	-0.07	-0.10	0.30	-0.02
1.25 km	0.84	0.26	-0.04	4.79	-1.30	-0.15	-0.10	0.27	0.03
1.15 km	0.77	0.17	-0.05	4.63	-1.08	-0.20	-0.11	0.24	0.08
1.05 km	0.70	0.06	-0.02	4.44	-1.03	-0.18	-0.13	0.20	0.13
0.95 km	0.64	-0.03	-0.00	4.15	-0.98	-0.17	-0.11	0.17	0.14
0.85 km	0.57	-0.11	-0.03	3.75	-0.84	-0.17	-0.07	0.13	0.15
0.75 km	0.46	-0.16	-0.09	3.31	-0.71	-0.16	-0.05	0.10	0.14
0.65 km	0.30	-0.15	-0.16	2.87	-0.62	-0.12	-0.05	0.08	0.11
0.55 km	0.19	-0.23	-0.16	2.38	-0.49	-0.08	-0.06	0.06	0.09
0.45 km	0.08	-0.31	-0.11	1.80	-0.29	-0.04	-0.07	0.03	0.07
0.35 km	-0.05	-0.32	-0.04	1.23	-0.11	-0.02	-0.06	0.02	0.03
0.25 km	-0.12	-0.24	0.03	0.75	-0.04	-0.02	-0.03	-0.01	0.01
0.15 km	-0.11	-0.11	0.07	0.34	-0.02	-0.01	-0.02	-0.01	0.01

VERTICAL VELOCITIES (m/s) -- ALLOWING DENSITY VARIATIONS

	2124Z	2120Z	2116Z	2112Z	2108Z	2101Z	2053Z	2048Z	2043Z
1.1 km	0.84	0.17	-0.07	4.65	-1.10	-0.20	-0.12	0.24	0.11
1.0 km	0.77	0.06	-0.05	4.36	-1.04	-0.18	-0.11	0.20	0.14
0.9 km	0.69	-0.02	-0.05	3.97	-0.94	-0.17	-0.08	0.16	0.15
0.8 km	0.59	-0.09	-0.10	3.51	-0.80	-0.17	-0.06	0.12	0.15
0.7 km	0.45	-0.11	-0.16	3.03	-0.68	-0.14	-0.04	0.09	0.13
0.6 km	0.31	-0.14	-0.20	2.53	-0.56	-0.10	-0.05	0.07	0.10
0.5 km	0.19	-0.22	-0.17	1.97	-0.39	-0.06	-0.06	0.05	0.08
0.4 km	0.07	-0.27	-0.11	1.38	-0.20	-0.03	-0.06	0.03	0.05
0.3 km	-0.03	-0.23	-0.04	0.84	-0.07	-0.02	-0.04	0.01	0.02
0.2 km	-0.06	-0.12	0.02	0.38	-0.02	-0.01	-0.02	-0.00	0.01

continuity equations. For both rainbands the differences are nearly negligible, thus establishing the incompressible assumption as a "good" assumption in this case.

To gauge the importance of boundary layer buoyant motions, an assessment of the convective available potential energy (CAPE) in that layer was undertaken. Holton (1992) shows a CAPE/buoyancy relationship as follows:

$$\begin{aligned} dw/dt &= g[(\rho_{env} - \rho_{parcel})/\rho_{parcel}] \\ &= g[(T_{v,parcel} - T_{v,env})/T_{v,env}] \end{aligned} \quad (7)$$

where dw/dt = the vertical acceleration due to buoyancy
 g = the acceleration due to gravity

$$\text{CAPE} = \text{work}_{\text{per unit mass}} = (\text{force}_{\text{per unit mass}})(\text{distance}) = (dw/dt)dz \quad (8)$$

Since CAPE in a given layer can be viewed as the maximum kinetic energy a rising buoyant parcel could obtain in that layer, a relationship to vertical velocity can be written:

$$\begin{aligned} (w_{max})^2/2 &= \text{CAPE} \\ \text{or} \end{aligned} \quad (9)$$

$$w_{max} = \sqrt{2g[(T_{v,parcel} - T_{v,env})/T_{v,env}]dz}$$

Calculations of the maximum CAPE-driven vertical velocities for each layer were done by averaging the environmental virtual temperatures up to that layer and averaging the parcel virtual temperatures up to the layer. Parcel virtual temperatures were determined using the saturated adiabatic lapse rate equation (Hobgood, 1992):

$$dT/dz = [(l_v q_v g)/(R_d T) + g]/[-(l_v^2 q_v M_v)/(T^2 R^*) - c_p] = - \Gamma_v \quad (10)$$

where l_v = the latent heat of vaporization
 q_v = the specific humidity
 T = the parcel virtual temperature
 M_v = the molecular weight of water vapor
 R^* = the universal gas constant
 c_p = the specific heat of the air at constant pressure

Specific humidities were obtained through vapor pressures calculated using the Goff-Gratch equation (List, 1984). The CAPE-driven maximum vertical velocity values are shown in Figures 25 (first rainband) and 26 (second rainband). As expected (due to the area of reduced cloudiness) there were some significant CAPE-driven vertical motions (up to 8 m s^{-1}) at the front of the first rainband. This analysis suggests vertical velocities up to 4 m s^{-1} at the back of the second rainband.

D. Discussion of Results

This section first addresses how well the analyses of the last section met the three-fold goal of that section. Also, as done by Gentry (1983), some of the derived information is applied to the vorticity equation to provide further clarification.

The helicity analysis highlighted the first rainband's lack of favorable tornadogenetic shear. This analysis also demonstrated that storm-relative helicity does not have to be calculated for depths more than 1500 m in highly sheared hurricane-induced tornado environments to produce values above

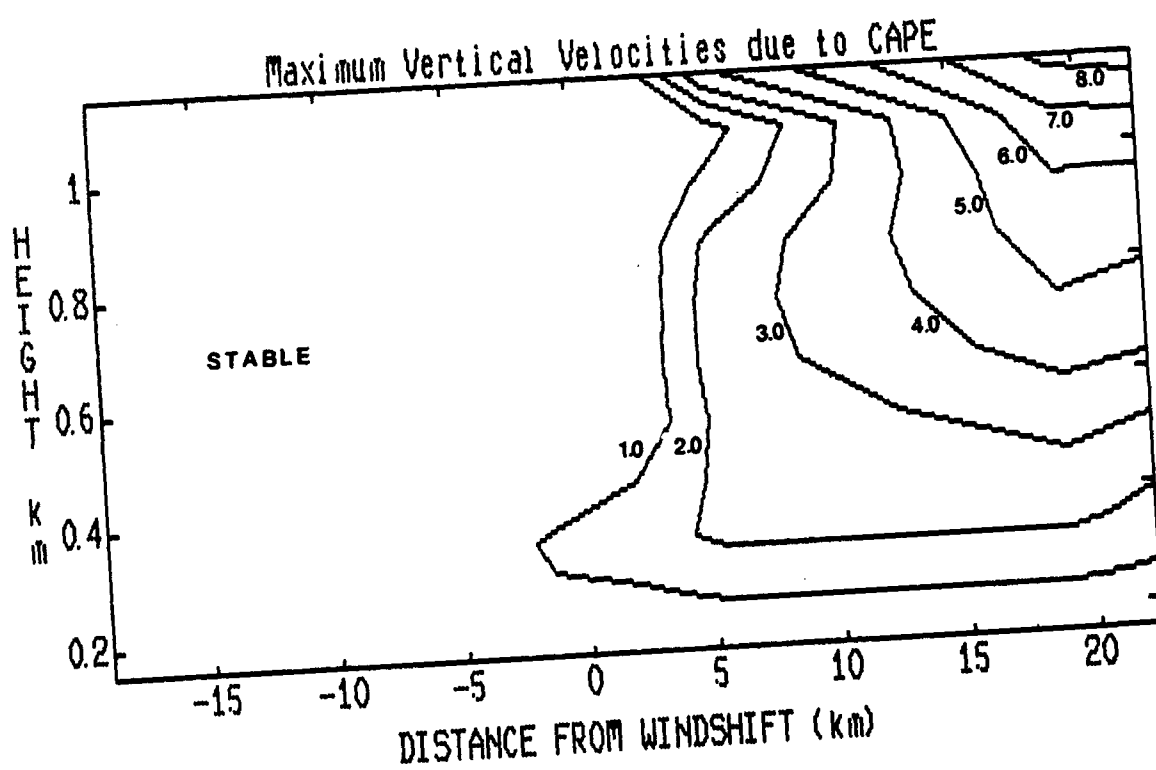


Figure 25. East-west cross section (looking north) of the maximum CAPE-induced upward velocities in the first rainband. Speeds are in m s^{-1} .

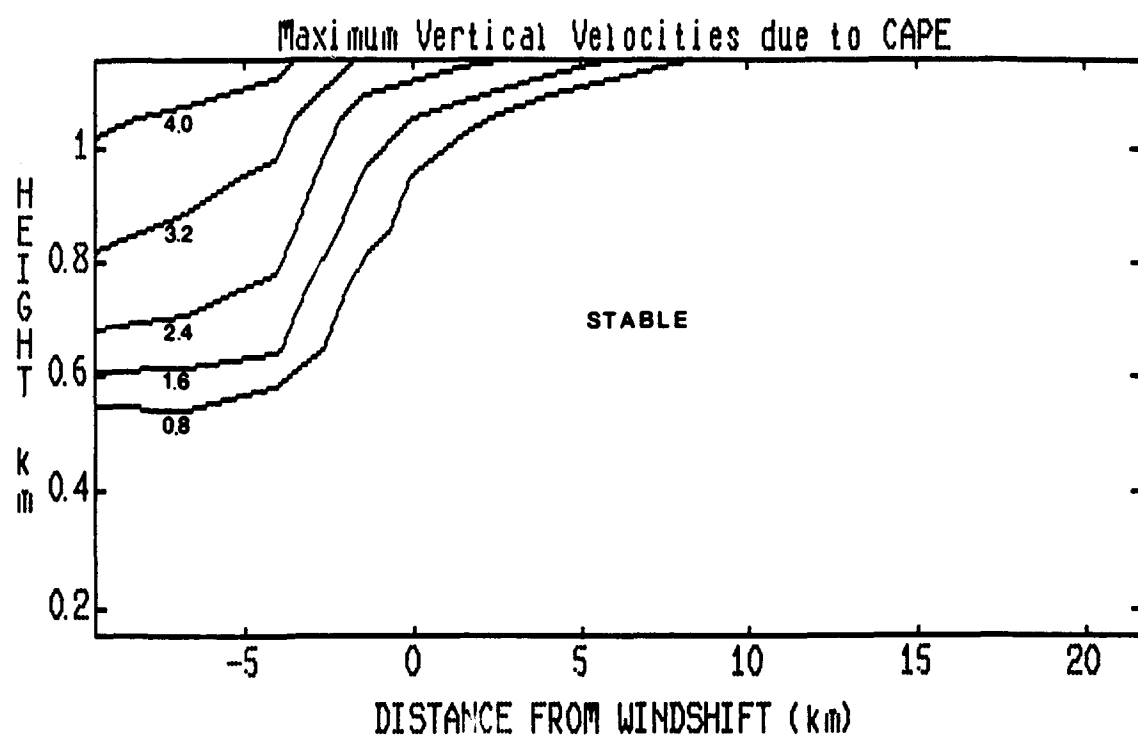


Figure 26. East-west cross section (looking north) of the maximum CAPE-induced upward velocities in the second rainband. Speeds are in m s^{-1} .

the 150 J kg^{-1} threshold for mesocyclone and tornado development. That the helicity in front of the second rainband windshift (Figure 20) indicated only weak, F0 and F1, tornado development is consistent with the F1 tornadoes that actually occurred with this rainband (see Figure 1). Perhaps most importantly, the highest values of helicity associated with the second rainband were out in front of the windshift in what can be considered the "inflow" region of the rainband.

The mass convergence analysis clearly shows a spike of upward vertical velocities associated with the second rainband windshift. This updraft exceeded 1 m s^{-1} at only 350 m AGL and increased rapidly to greater than 5 m s^{-1} at 1500 m. With such significant vertical velocities as 1 to 5 m s^{-1} within the lowest 1500 m, the windshift must be considered a favored location for the tilting of shear-produced horizontal vorticity. This is consistent with the MGM radar documentation of tornado cyclones along the windshift boundary, below 1.8 km. While the presence of this updraft is difficult to discern in the lowest 1500 m in the hydrometeor vertical motion plot for the second rainband (Figure 6), Figure 24 demonstrates that the mass convergence-induced vertical velocities continued up through the 4 km level--right where the bright band disruption took place. Figure 24 indicates maximum velocities in this updraft to be slightly in excess of 8.0 m s^{-1} between 3 and 4 km AGL, or just enough to equal the fall speeds depicted in much of Figure 6.

Undoubtedly, however, above 3 km the convergence vertical velocities were kicking off convection that was probably enhancing the strength of the upward motion at the bright band. In fact the 27/1200 UTC CKL sounding indicated a level of free convection (LFC) at about 1.5 km.

The CAPE/buoyancy analysis showed that the first rainband derived more low-level upward motion through CAPE than it did through convergence at its windshift (Figures 21, 23, and 25). However, the first rainband was non-tornadic. The second, tornadic, rainband clearly gained more vertical motion in the region below 1500 m from convergence at the windshift than it did from buoyancy (Figures 22, 24, and 26). Additionally the buoyancy that was present in the second rainband coincided with the least tornadogenetic helicities. Further evidence of the existence of the windshift updraft is the "high" mode data indicating much slower hydrometeor fall speeds, $3-4 \text{ m s}^{-1}$ as opposed to $6-8 \text{ m s}^{-1}$, from 0.3 to 3.0 km AGL at the time of the windshift (this was mentioned in section B).

That the windshift-driven spike of upward vertical motion was so thin that it almost evaded profiler detection, may actually be favorable for mesocyclone and tornado formation. When Gentry (1983) performed his scale analysis on the vorticity equation,

$$\begin{aligned}
 \partial\zeta/\partial t = & -\mathbf{v} \cdot \overset{(1)}{\nabla}(\zeta + f) - (\partial u/\partial x + \overset{(2)}{\partial v/\partial y})(\zeta + f) \\
 & + [\overset{(3)}{\partial p/\partial x} \overset{(4)}{\partial \alpha/\partial y} - \overset{(3)}{\partial p/\partial y} \overset{(4)}{\partial \alpha/\partial x}] + [\overset{(4)}{\partial u/\partial z} \overset{(5)}{\partial w/\partial y} - \overset{(4)}{\partial v/\partial z} \overset{(5)}{\partial w/\partial x}] \\
 & + f(F)
 \end{aligned} \tag{11}$$

where ζ = relative vorticity about a vertical axis
 f = planetary vorticity about a vertical axis
 p = pressure
 α = specific volume
 $\partial\zeta/\partial t$ = time rate of change of relative vorticity
(1) = the advection term
(2) = the divergence term
(3) = the solenoid-like term
(4) = the tilting term
(5) = the frictional dissipation term

he showed term (4), the tilting term, to be the most significant with values ranging up to $2.5 \times 10^{-4} \text{ s}^{-2}$. As can be seen from Figure 14, Gentry's estimate of vertical velocity changes of -5 to 5 m s^{-1} over a distance of 500 m ($\partial w/\partial x = 2.0 \times 10^{-2} \text{ s}^{-1}$) is not an unreasonable one--especially in light of the divergence-induced downdraft depicted immediately adjacent to and in front of the updraft in Figure 22. However, because of smoothing, Figure 22 does yield a more conservative estimate of $\partial w/\partial x$ at $5.0 \times 10^{-3} \text{ s}^{-1}$ (note that because north-south wind variations are neglected in this analysis, $\partial w/\partial y$ is zero). Figure 4 suggests $\partial v/\partial z$ values up to $1.0 \times 10^{-2} \text{ s}^{-1}$. This gives a tilting term value for the second rainband of $5.0 \times 10^{-5} \text{ s}^{-2}$.

Gentry was only able to hypothesize that under intense rainband convection a value of $2.5 \times 10^{-5} \text{ s}^{-2}$ for term (2), the divergence term, could presumably be attained. The data presented here suggest his guess was a good one. Given that a 1500 m column would be affected by the windshift updraft for at least 100 s, tilting would produce a ζ of $\sim 5.0 \times 10^{-7} \text{ s}^{-1}$. This coupled with a divergence value, $-\partial u/\partial x$, of $\sim 4.4 \times 10^{-3}$

s^{-1} , yields a value of $2.2 \times 10^{-5} \text{ s}^{-2}$ --very similar to Gentry's term (2).

Term (3), the solenoid-like term, can be a significant producer of horizontal vorticity near the surface (Rotunno and Klemp, 1985), but the horizontal variations of virtual temperature in this case were far too small for this term to have bearing. Following Gentry's lead, terms (1), (3), and (5) are not considered important in this analysis for the concentration of vertical vorticity.

Combining terms (2) and (4) gives $\partial\zeta/\partial t$ a value of $7.2 \times 10^{-5} \text{ s}^{-2}$. This implies that the shear, convergence, and vertical velocities in the lowest 1500 m of the second rainband alone could produce mesocyclonic vorticity values ($\sim 10^{-2} \text{ s}^{-1}$) in less than 2.5 minutes. That this analysis shows terms (2) and (4) to be nearly the same magnitude, is in line with the characteristics documented for mesocyclonically produced Great Plains tornadoes (Davies-Jones, 1986). Furthermore, the almost equal interplay between the divergence and tilting terms in the second rainband of this study suggests a major difference between hurricane-tornadoes in general and the non-supercell tornadoes documented by Wakimoto and Wilson (1989). While hurricane-spawned tornadoes tend to be shallow and weak (F0-F2) like non-supercell tornadoes, Wakimoto and Wilson showed the latter to be mainly the result of vertical stretching and amplification of pre-existent vertical vorticity. Thus, the production of vertical

vorticity via tilting in tornadic hurricane rainbands appears to classify hurricane-tornadoes as fundamentally more similar to supercell tornadoes.

CHAPTER V

SUMMARY AND CONCLUSIONS

The hypothesis put forward in Chapter I stated that boundary layer convergence zones, rather than convective updrafts, are the primary mechanism by which horizontal vorticity is turned vertical in the hurricane-induced tornado environment. The following evidence was presented that supports the above argument:

- 1) Both the Doppler radar photographs of the MGM region and the UAH profiler data documented the passage of a strong windshift near the center of a tornadic rainband. Both the radar and profiler data indicated that most of the convergence associated with this windshift occurred below 1500 m AGL.
- 2) The Doppler radar photographs showed mesocyclone signatures only along the windshift boundary.
- 3) A continuity analysis of the UAH profiler data showed that convergence at the windshift of the tornadic rainband could produce a 5.0 m s^{-1} updraft of limited horizontal extent within the lowest 1500 m AGL.

- 4) Storm-relative helicity values for the lowest 1500 m exceeded the Davies-Jones et al. (1990) threshold of 150 J kg^{-1} for mesocyclone-produced tornadoes in the inflow region of the tornadic rainband windshift.
- 5) An analysis of boundary layer (below 1.1 km) CAPE indicated that the inflow region of the tornadic rainband was stable; buoyant upward motions of up to 4 m s^{-1} were possible behind the windshift where the helicity values were lowest ($\sim 50 \text{ J kg}^{-1}$). Possible buoyant upward motions of up to 8 m s^{-1} did characterize the boundary layer inflow region of the non-tornadic rainband.
- 6) A vorticity equation analysis demonstrated that mesocyclonic magnitudes of vorticity (10^{-2} s^{-1}) could be produced in a 1500 m column of air that lingered for more than 2 minutes in the updraft and convergence of the tornadic rainband windshift.

One of the more imposing questions that remain is what causes the windshift? In the case of the tornadic rainband presented here, the windshift quite possibly could have been a manifestation of the low-level inflow into the convection occurring above the LFC. Or the windshift may have been the initial trigger in a conditionally unstable environment. In any case, while CAPE may have been unimportant at the lowest

levels in the cases presented here, it still must be considered a key parameter in hurricane-induced tornado studies. It is interesting to note, however, that a mesoscale windshift of any sort, even one of a topographic nature, could have created convergence and vertical velocities in the lowest 1500 m very similar to those seen in this work.

The arguments presented here offer a plausible mechanism for the formation of mesocyclones in the landfalling hurricane environment. It is assumed that these mesocyclones represent the initial low-level circulations that later become tornadoes. It is speculated that owing to their low-level nature, hurricane mesocyclones can more easily than their mid-level Great Plains counterparts interact with the ground in the method described by Smith and Leslie (1979) to produce tornadoes.

LIST OF REFERENCES

Barcilon, A. I., and P. G. Drazin, 1972: Dust devil formation. *Geophysical Fluid Dynamics*, 4, 147-158.

Davies-Jones, R. P., 1986: Tornado dynamics. In *Thunderstorms: A Social and Technological Documentary*, Vol. II. E. Kessler, (Ed), Second Edition revised and enlarged, University of Oklahoma Press, Norman, OK and London, 197-236.

Davies-Jones, R. P., D. Burgess and M. Foster, 1990: Test of helicity as a tornado forecast parameter. *Preprints, 16th Conf. Severe Local Storms, Kananaskis, Alberta, Amer. Meteor. Soc.*, 588-592.

Fujita T. T., 1963: Analytical mesometeorology: A review. *Meteor. Monogr.*, No. 27, Amer. Meteor. Soc., 77-125.

Fujita T. T., K. Watanabe, K. Tsuchiya, and M. Shimada, 1972: Typhoon-associated tornadoes in Japan and new evidence of suction vortices in a tornado near Tokyo. *J. Met. Soc. Japan*, 50, 431-453.

Fujita T. T., 1973: Tornadoes around the world. *Weatherwise*. 26, 56-83.

Gentry, R. C., 1983: Genesis of tornadoes associated with hurricanes. *Monthly Weather Review*. 111, 1793-1805.

Hill, E. J., W. Malkin, and W. A. Schulz, 1966: Tornadoes associated with cyclones of the tropical origin--practical features. *Journal of Applied Meteorology*. 5, 745-63.

Hoadley, D. K., 1981: A Tropical Storm David tornado in Fairfax County--September 1979. *Bull. Amer. Meteor. Soc.* 62, 498- 507.

Hobgood, J. S., 1992: Atmospheric Science 631 class notes. Atmospheric Science Program, Department of Geography, The Ohio State University.

Holton, J. R., 1992: *An Introduction to Dynamic Meteorology*. Third Edition. Academic Press. 511 pp.

Johnson, K. W., P. S. Ray, B. C. Johnson, and R. P. Davies-Jones, 1987: Observations related to the rotational dynamics of the 20 May 1977 tornadic storms. *Mon. Wea. Rev.* 115, 2463-2478.

Knupp, K. R., 1993: The 915 MHz Profiler System. University of Alabama in Huntsville information packet.

Leslie L. M., 1971: The development of concentrated vortices: a numerical study. *J. Fluid Mech.* 48, 1-21.

Lilly, D. K., 1986: The structure, energetics, and propagation of rotating convective storms. Part II: Helicity and storm stabilization. *J. Atmos. Sci.* 43, 126-140.

List, R. J., 1984: *Smithsonian Meteorological Tables*. Fifth Reprint. Smithsonian Institution Press. 527 pp.

McCaul, E. W., Jr., 1987: Observations of the Hurricane "Danny" tornado outbreak on 16 August 1985. *Mon. Wea. Rev.*, 115, 1206-1223.

McCaul, E. W., Jr., 1991: Buoyancy and shear characteristics of hurricane-tornado environments. *Mon. Wea. Rev.*, 119, 1954-1978.

McCaul, E. W., Jr., K. R. Knupp, and W. L. Snell, 1993: Observations of tornadic storms and rainbands within Hurricane Andrew's remnants. *Preprints, 17th Conf. Severe Local Storms*. St Louis, MO. Amer. Meteor. Soc. In press.

Novlan, D. J. and W. M. Gray, 1974: Hurricane spawned tornadoes. *Monthly Weather Review*. 102, 476-88.

Orton, R., 1970: Tornadoes associated with Hurricane Beulah on September 19-23, 1967. *Monthly Weather Review*. 98, 541-47.

Ostby, F. P. and S. J. Weiss, 1993: Tornadoes associated with Hurricane Andrew. *Preprints, 13th Conf. Weather Analysis and Forecasting*. Amer. Meteor. Soc. 490-493.

Pearson, A. D. and A. F. Sadowski, 1965: Hurricane-induced tornadoes and their distribution. *Mon. Wea. Rev.* 93, 461- 464.

Rotunno, R., and J. B. Klemp, 1985: On rotation and propagation of simulated supercell thunderstorms. *J. Atmos. Sci.* **42**, 271-292.

Rudd, M. I., 1964: Tornadoes during Hurricane Carla at Galveston. *Mon. Wea. Rev.* **92**, 251-254.

Smith, J. S., 1965: The hurricane-tornado. *Monthly Weather Review*. **93**, 453-459.

Smith, R. K., and L. M. Leslie, 1979: A numerical study of tornadogenesis in a rotating thunderstorm. *Q. J. R. Meteorol. Soc.* **105**, 107-127.

Stiegler, D. J. and T. T. Fujita, 1982: A detailed analysis of the San Marcos, Texas, tornado induced by Hurricane "Allen" on 10 August 1980. *Preprints, 12th Conf. Severe Local Storms*, San Antonio, Amer. Meteor. Soc. 371-374.

Wakimoto, R., and J. W. Wilson, 1989: Non-supercell tornadoes. *Monthly Weather Review*. **117**, 1113-1140.

Wilson J. W., G. B. Foote, N. A. Crook, J. C. Fankhauser, C. G. Wade, J. D. Tuttle, C. K. Mueller and S. K. Krueger, 1992: The role of boundary-layer convergence zones and horizontal roles in the initiation of thunderstorms: a case study. *Mon. Wea. Rev.*, **120**, 1785-1815.